Air Force Institute of Technology

AFIT Scholar

3-14-2007

Anisotropy in the South Atlantic Anomaly

Shaun M. Easley

Follow this and additional works at: https://scholar.afit.edu/etd

Part of the Atmospheric Sciences Commons

Recommended Citation

ANISOTROPY IN THE SOUTH ATLANTIC ANOMALY

THESIS

Shaun M. Easley, Captain, USAF

AFIT/GAP/ENP/07-02

DEPARTMENT OF THE AIR FORCE
AIR UNIVERSITY

AIR FORCE INSTITUTE OF TECHNOLOGY

Wright-Patterson Air Force Base, Ohio

AFIT/GAP/ENP/07-02

ANISOTROPY IN THE SOUTH ATLANTIC ANOMALY

THESIS

Presented to the Faculty

Department of Engineering Physics

Graduate School of Engineering and Management

Air Force Institute of Technology

Air University

Air Education and Training Command

In Partial Fulfillment of the Requirements for the

Degree of Master of Science in Applied Physics

Shaun M. Easley, BS
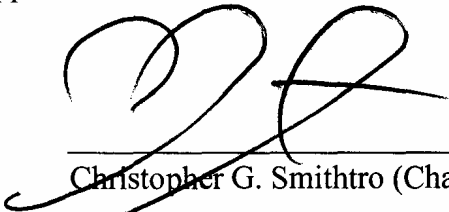
Captain, USAF

March 2007

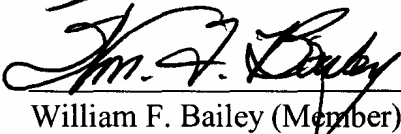APPROVED FOR PUBLIC RELEASE; DISTRIBUTION UNLIMITED

AFIT/GAP/ENP/07-02

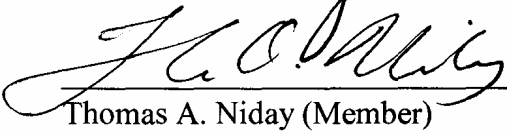ANISOTROPY IN THE SOUTH ATLANTIC ANOMALY

Shaun M. Easley
Captain, USAF

Approved:

_____
Christopher G. Smithtro (Chairman)

14 Mar 07
_____
Date

_____
William F. Bailey (Member)

14 Mar 07
_____
Date

_____
Thomas A. Niday (Member)

14 Mar 07
_____
Date

AFIT/GAP/ENP/07-02

Abstract

The South Atlantic Anomaly (SAA) is an area of increased radiation that poses a danger to satellites and manned spacecraft. From June 2000 through July 2006, the TSX-5 satellite measured proton fluxes in the SAA using its CEASE instrument. A review of the satellite data by scientists at AFRL/VSBX revealed an unanticipated, recurring bi-modal structure in histograms of the proton counts. This research identified the bi-modal behavior as anisotropic in nature, and the result of two separate processes. At low altitudes the anisotropy was well described by the classic "East-West Effect." Comparisons of the satellite data to simple analytical models are presented. At high altitudes, the anisotropy was the result of the detector measuring protons at different pitch angles when looking east vs. west. The sampled pitch angles were also found to be function of location, leading to a latitudinal variation to this anisotropy. Finally, we also examined a series of unusually high readings that affected some of the statistics in this study. These anomalous counts were found to have a possible solar cycle dependence leading to questions about the suitability of the current time-independent scheme used to sort the satellite's data set. Other possible explanations for the anomalous counts are also presented.

To my wife,

with gratitude for her patience and encouragement

Acknowledgments

Table of Contents

List of Tables

ANISOTROPY IN THE SOUTH ATLANTIC ANOMALY

I. Introduction

1.1. Motivation

As satellites travel around the Earth in low altitude orbits (~400-700 km altitude), they experience a localized increase in radiation over the South Atlantic, called the "South Atlantic Anomaly" (SAA). This increased radiation dose can damage satellites and reduce their operational effectiveness. A common solution to the problem is to reduce the satellite's power while traveling through the SAA, based upon models of where the radiation will be.

For several years now, researchers have known that some of the radiation models are incorrectly identifying the location of the SAA. Changes in the Earth's magnetic field have led to changes in the anomaly's location that have been difficult to account for. This had led to is an interest in trying to create an improved dynamic model based upon new measurements of the SAA taken by the Tri-Service eXperiment 5 (TSX-5) satellite.

Some unanticipated and problematic patterns emerged in the TSX-5 data set, however, which needed to be resolved before development of the model can proceed. The purpose of this research is to identify the sources of those patterns.

1.2. Overview

The first step in trying to accomplish this research was a background investigation into the various facets of South Atlantic Anomaly. Section 1.3.1 describes the source of the anomaly, as well as some of the impacts that the SAA can have upon satellites and humans. That section also contains information on changes that have been occurring within the SAA and what is

causing those changes. This leads to a discussion on various attempts to model the SAA in Section 1.3.2, with particular emphasis placed on AFRL/VSBX's SAAMAPS model. This model is a result of satellite observations taken aboard the TSX-5 satellite from 7 June 2000 to 1 July 2006. Section 1.3.3 will discuss the nature of the satellite's mission as well as some of the instrumentation used to collect the data.

From here, we take a preliminary look at the data itself in Section 1.3.4. Specifically, this research is interested in explaining why there appears to be two separate Gaussian distributions in many of the histograms of the TSX-5 satellite data. The hypothesis was that these separate distributions were a product of the "East-West Effect," a well-understood behavior of the SAA which will be explained in Section 1.3.5. In reality, the East-West Effect was only partly responsible for the different profiles. A "pitch angle difference" effect was also observed. The fundamental physics of this second effect are explained in Section 1.3.6.

Chapter 2 describes the various procedures that were used to identify the sources of the anisotropy in the SAA. The first step in this process was to prepare the data for use by sorting it into a geographic arrangement. This procedure is described in Section 2.1.1. In Section 2.1.2, a method of sorting measurements between eastward flux and westward flux is presented. This section goes on to describe how the eastward and westward flux data was compared to determine if any anisotropic behavior was present. Section 2.1.3 describes the error evaluation techniques used to study the reliability of these comparisons. After both of these elements were in place, a method of studying anisotropy across altitudes is presented in Section 2.1.4 Then, Section 2.1.5 describes how an analytical model of the East-West Effect was created, so that measured values of the East-West Effect could be compared to the theoretically predicted values. Finally, Section 2.2 expands upon this by briefly describing the resources needed to accomplish this research.

In Chapter 3, we begin discussing the results of the research. First, Section 3.1 confirms

that the different radiation profiles observed by AFRL/VSBX were, in fact, the result of an anisotropy with east and west components. This leads to a discussion on the pitch angle difference effect in Section 3.2. Of particular interest is the variability of the satellite's pitch angle in relation to the satellite position at the time of measurement. It was this relationship that allowed the pitch angle difference effect to be understood, and that allowed studies of both forms of anisotropy to occur. The East-West Effect is discussed in Section 3.3, making use of comparisons to the results of the analytical model developed in Section 2.1.5. This comparison leads us to claim that the East-West Effect is being measured within the SAA, with some degree of accuracy. This claim is further supported by an analysis of how the anisotropies are affected by the energy levels of the various protons, as presented in Section 3.4. We end the chapter with a sidebar on statistical problems encountered throughout the research, and possible causes of these problems, to include solar cycle variability and satellite orientation problems. This work is presented in Section 3.5.

All of these aspects will be covered again in Section 4.1, which lays out the conclusions of the research. Section 4.2 discusses how the results of the research tie into AFRL/VSBX's SAAMAPS endeavor, while Section 4.3 lists areas of future study that could be conducted based upon the results of this research.

1.3. Background Information:

1.3.1.   *The South Atlantic Anomaly*

The South Atlantic Anomaly is a feature of the Earth's radiation belts brought about by a localized minimum in the Earth's magnetic field [*Heirtzler*, 2002]. The anomaly consists of charged particles whose motion can be described by "adiabatic invariants," orbital motion about a magnetic field line such that the radius of rotation always encloses a constant amount of magnetic flux [*Sturrock*, 1994]. Sturrock goes onto show that there are different types of invariants based

upon the nature of the magnetic field line being orbited. For instance, the third invariant shows that, for a magnetically stable environment, particles will drift around the Earth such that they maintain a constant magnetic flux from the Earth's magnetic field inside.
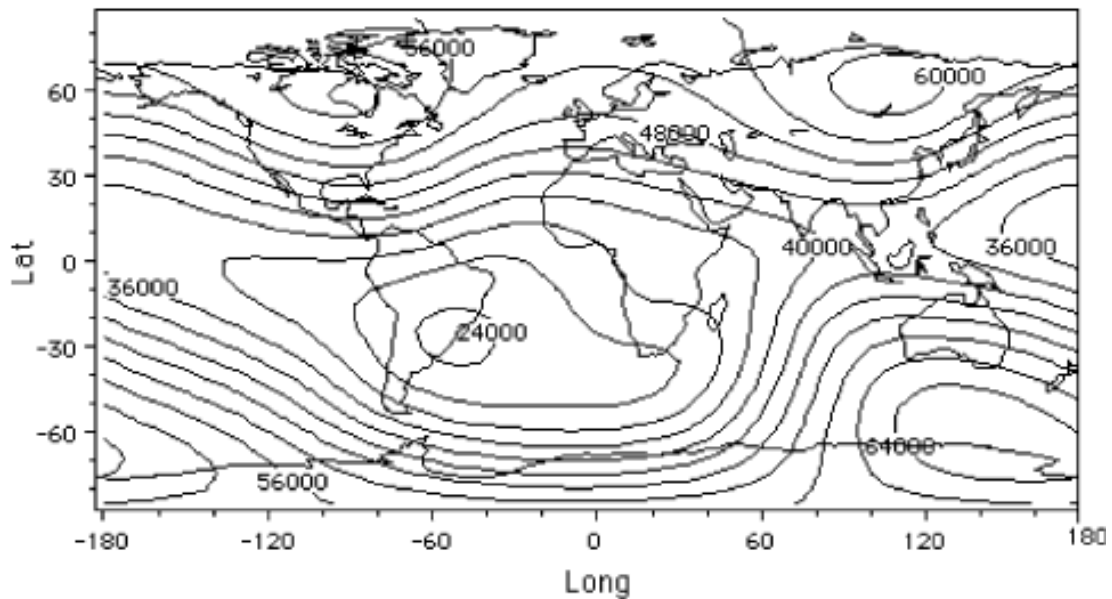
Figure 1.1: Intensity in nT of the Earth's geomagnetic field in 1995 at the Earth's surface [Heirtzler, 2002]

If the Earth's magnetic field were a geodetically-centered dipole, the third invariant would give rise to circular orbits centered about the Earth's core. In reality, the Earth's magnetic field is best described by a constantly changing set of spherical harmonics [*Heirtzler*, 2002]. As such, localized minima and maxima in the strength of the Earth's magnetic field can occur, as seen in Figure 1.1. For a proton following the third adiabatic invariant, its altitude will increase or decrease to maintain a constant magnetic field inside its orbit. The weak magnetic field over the South Atlantic will cause a proton to descend in altitude in order to follow the third adiabatic invariant. That means that the point of closest approach to the Earth generally occurs above the South Atlantic Ocean off the coast of Brazil.

This becomes a concern because the radiation belts contain large numbers of highly energized electrons and protons with energies anywhere from 1 keV to 100 MeV [*Cravens*,

1997]. Because of the weak magnetic field strength over the South Atlantic, these high energy particles are often found at altitudes consistent with low Earth orbit satellites' trajectories and the International Space Station (ISS) [*Badhwar et al.,* 1999]. This effect can be clearly seen in Figure 1.2, which shows the average flux of protons between 400 and 450 km altitude with energy between 25-120 MeV that were observed by TSX-5 over nearly the first five years of its mission. Over the South Atlantic and South America, the satellite observed proton fluxes nearly three orders of magnitude higher than everywhere else on the globe at the same altitude range.
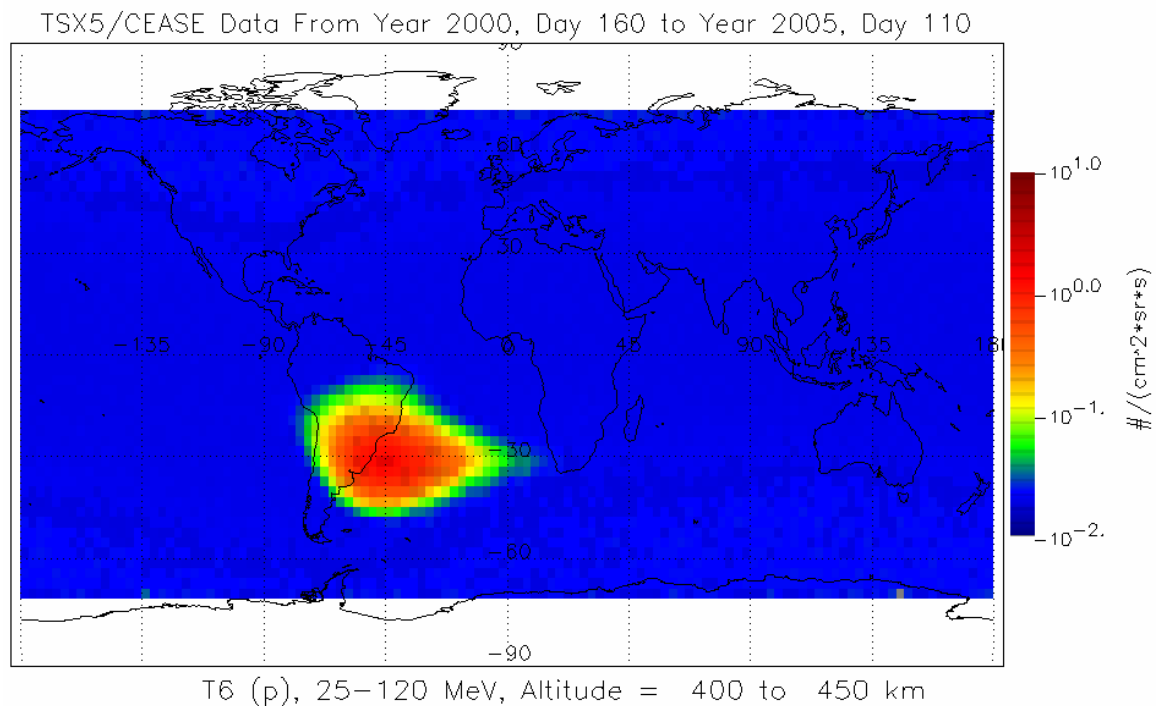
Figure 1.2: Contour plot of >25 MeV proton counts between 400 and 450 km altitude as observed by the TSX-5 satellite over the first ~5 years of its mission (G. Ginet, private communication, 2006)

When these high-energy protons collide with satellites, they can potentially interfere with the crafts' solar cells and electronics [*Heirtzler,* 2002]. These collisions degrade the performance of solar cells permanently, reducing available power for satellite operations. These same particles can also cause single event upsets in a satellite's electronics, leading to faulty data or errors in

instructions being performed [*Heirtzler*, 2002]. Potential solutions to these problems include reducing power usage in high flux environments or adding shielding to critical satellite components. Shielding adds weight to the satellite, however, and increased mass can significantly drive up launch costs. On the other hand, reducing power usage may result in a temporary loss of operational capability, as happens with the Hubble Space Telescope everytime it travels through the SAA [*Heirtzler*, 1999].

1.3.2. Modeling the South Atlantic Anomaly

To reduce the amount of operational down time for any vehicle passing through the SAA, it is useful to have a model of the proton density within the region. Several models of the radiation belts currently exist (AE8, AP8, AP8MAX, and SEEMAPS), but these models can incorrectly identify the intensity and locaiton of the SAA, because they do not take into account on-going changes in the Earth's magnetic field [*Daly et. al*, 1996].

Complicating the situation, Heirtzler [2002] showed that these changes are not uniform and that certain regions (including the SAA) can experience comparatively rapid changes in magnetic field strength over a period of time. For instance, the magnetic field around the SAA was found to decrease anywhere from 25.2 nT/year up to 110 nT/year, as shown in Figure 1.3. In addition to a weakening of the magnetic field throughout the SAA, the non-uniform nature of the weakening has led to a westward drift in the SAA's location [*Heynderickx*, 1996]. This means that models based upon old data will incorrectly identify the current parameters (intensity, location, etc.) of the Anomaly.
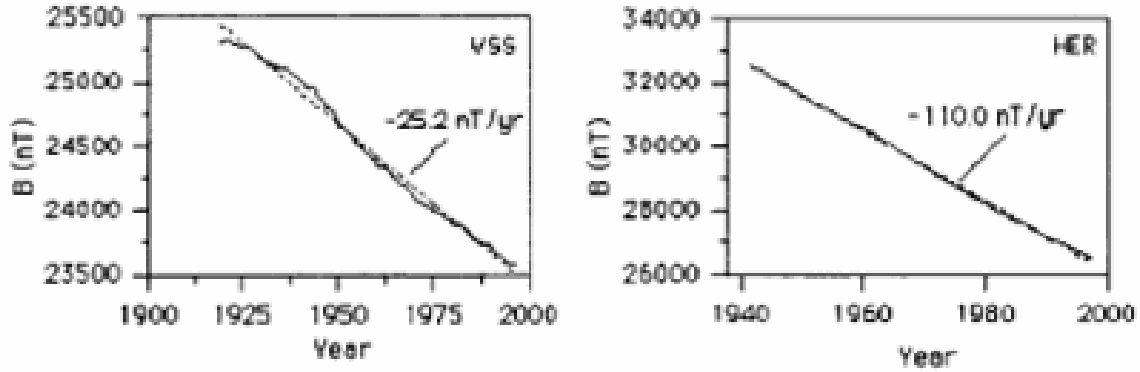
Figure 1.3: Annual variation in the Earth's magnetic field strength at Vassouras, Brazil (VSS) and Hermanus, South Africa (HER) [*Heirtzler*, 2002]

For instance, Figure 1.4 shows that in 1990, STS-31 measured the peak radiation dose within the SAA at a longitude 6.8° westward of where it was predicted by the AP-8Max model, which was based on data from 1970. This can lead to operational issues, since satellites and spacecraft would be operating in a high-energy environment earlier than expected.
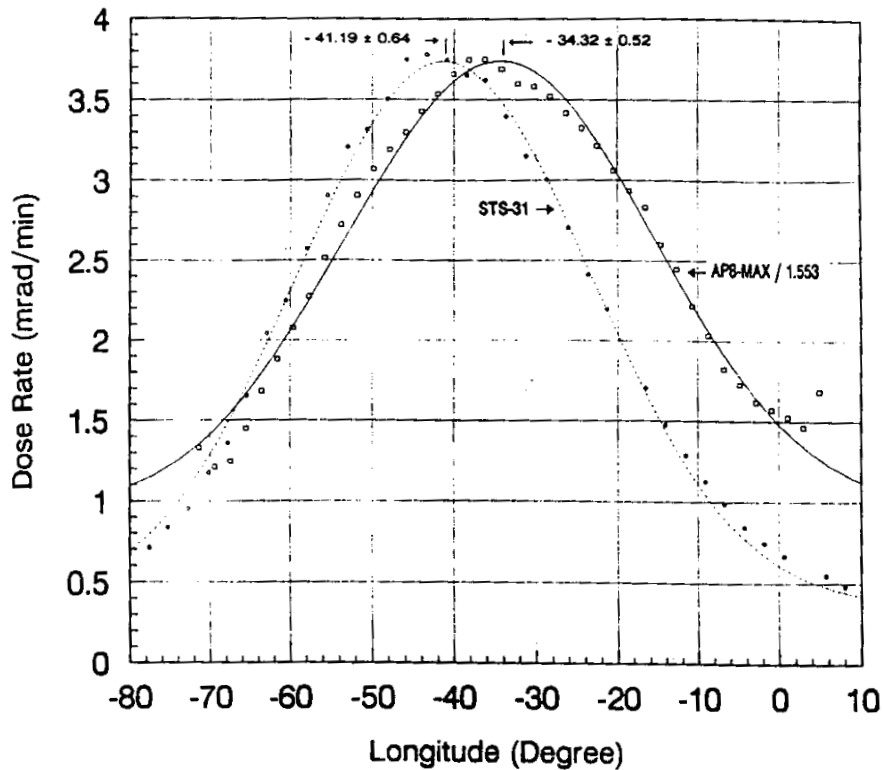
Figure 1.4: Longitude of peak radiation dose within the SAA as predicted by AP8-Max model and measured by STS-31 [*Konradi et. al,* 1994]

To correct for the problem of SAA drift in the current models, AFRL/VSBX proposed the development of a model called SAAMAPS. This model would provide average proton flux values for a range of altitudes from 400km to 1650 km. To account for the SAA's dynamic behavior, particle counts from an operational satellite, such as POES, would be used as input conditions for models of the fluxes throughout the anomaly. Since POES orbits in a relatively limited altitude range, a means of extrapolating fluxes with respect to altitude must first be developed. This has recently been made possible by the data obtained from the CEASE instrument onboard TSX-5.

1.3.3. *Tri-Service eXperiment 5 and the Compact Environmental Anomaly Sensor*

TSX-5 was launched on 7 June 2000 into a highly elliptical orbit (410 km perigee, 1710 km apogee, and 86° inclination) [*Brautigam et al*., 2001] carrying it through the South Atlantic Anomaly at various altitudes, latitudes, and longitudes. It collected its final data on 1 July 2006, resulting in over 6 years of nearly continuous data. During this time, the satellite was kept in a spin-stabilized orbit such that TSX-5's orientation was roughly the same each time it passed through a certain region of space.

On board, TSX-5 carried the Compact Environmental Anomaly SEnsor (CEASE), which measured particle fluxes over a wide range of proton and electron energies [*Brautigam et al*., 2001]. CEASE is a commercial sensor developed by Amptek, which according to their website (http://www.amptek.com/cease.html) is designed to provide satellite operators with "real-time warnings that the environment is likely to cause [satellite] anomalies." This would allow operators to put satellites into a safe mode during instances when the space environment might be hazardous to certain electronic systems on board.

Instead of using it for this application, the scientists at AFRL/VSBX used it as a scientific instrument to collect a wide range of space weather data. Specifically, CEASE has two

instruments that allow it to collect data on particle populations in Earth's orbit – the dosimeters and the telescope.
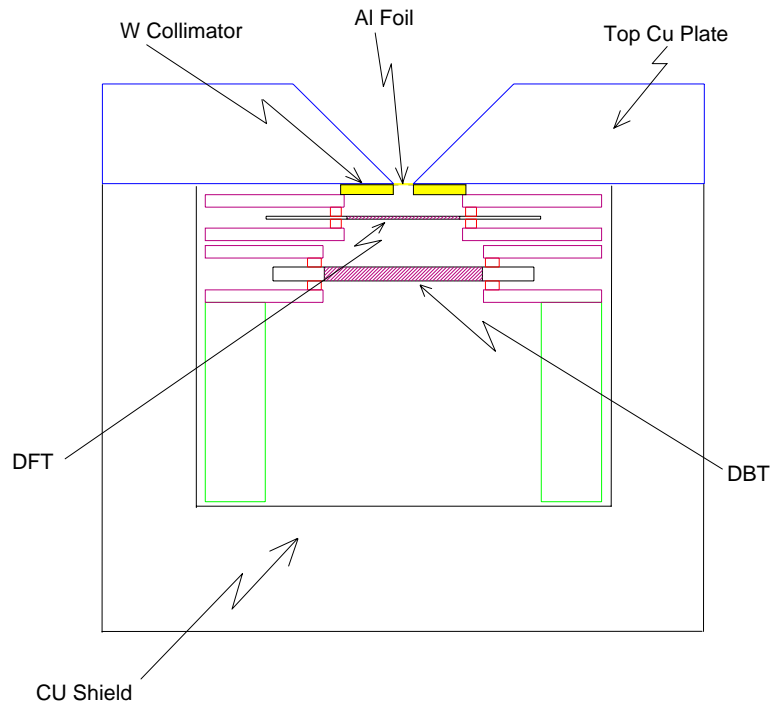
Figure 1.5: Schematic of CEASE telescope [*Redus et al.*, 2004]

Of primary interest to this work is the CEASE telescope. The article by *Brautigam et al.* [2006] describes the CEASE telescope as two solid state detectors surrounded a copper shield. One side of the shield is a copper plate giving way to a tungsten collimator covered by aluminum foil designed to filter out low-energy particles. Inside the telescope, the two solid state detectors are stacked one in front of the other as shown in Figure 1.5. Particles are detected after they enter through the tungsten window (or the copper plate if they have enough energy) and strike the front detector (DFT). The energy deposited by the particle as a result of the strike, will be counted in one of eight pre-defined energy ranges for the DFT. If the particle has a sufficiently high energy, it may pass through the back of the front detector and strike the back detector (DBT).   Any reading by the DBT within 500 nsec of a reading on the DFT is defined as the measurement of a

single particle. The DBT also uses an eight energy range scheme to measure particles, albeit with different energy values.

To determine how much energy the particle actually had, energy range data from the DFT is combined with energy range data from the DBT (if there was any) to assign the particle into one of 64 possible energy ranges. The method for combining DBT and DFT values to determine the energy range is explained in detail by *Brautigam et al.* [2006]. Table 1.1 summarizes the results for five specific energy channels, T5-T9, that were used extensively throughout this research. As an example, it shows that the T5 channel is capable of measuring protons with energy values from 10 MeV up to 100 MeV.

Table 1.1: Energy ranges of measured protons for CEASE channels T5-T9

Channel Name	Energy range of protons
T5	10-100 MeV
T6	25-120 MeV
T7	40-200 MeV
T8	70-200 MeV
T9	>59 MeV

Data collection was accomplished through a 5-second collection time. In other words, each channel records the number of protons within its specific energy range that struck the detector over a 5-second period. This 5-second measurement is then recorded in the data along with a time-stamp of the measurement. For instance, a T5 value of 0.2 counts/second would indicate that CEASE measured one proton between 10 and 100 MeV within that given 5-second period.

Ultimately, the 5-second, channeled counting scheme forms the basis of the data set used throughout this research. While the count does not represent a flux *per se*, it is related to the flux in that a large count indicates that the satellite experienced a high flux in that 5 second period, while a low count means the satellite measured a low flux. Conversion between counts and fluxes are possible, but any conversion must take into account the field of view of the detector,

10

the ability of the detector to measure protons, and several other issues. For simplification, these issues are expressed as a simple geometric factor. However, the conversion is complicated in that the geometric factors for the different channels are not the same. Furthermore they must be calculated using Monte Carlo simulations. As of the time of this publication, the geometric factors have not been finalized, meaning that all measurements are reported as counts/second rather than the fluxes that would be traditionally used.

Another issue for consideration is the organization of the data. CEASE collected 5-second intervals of data throughout nearly the entire 6-year span of the mission. These results were stored chronologically, leading to the need to reorganize the data into an arrangement more suitable for studying geographic features such as the South Atlantic Anomaly. To accomplish this, AFRL/VSBX devised a scheme where the data was sorted into geodetic "bins" of 3 degrees latitude by 3 degrees longitude by 50 km altitude. AFRL/VSBX determined that boxes of this size should be sufficiently small so as to minimize the impact of the internal variations in latitude, longitude, and altitude, while simultaneously providing a sample size large enough for statistical purposes (G. Ginet, private communication, 2006). This would later be called into question over the course of this research, as seen in Section 3.5.

In sorting the data into geodetic bins, any day with a solar proton event, as defined by NOAA's Space Environment Services Center (SESC), were filtered out. SESC defines a solar proton event as the first of at least three consecutive five-minute averages of >10 MeV protons where the average proton rate is >10 protons/cm^2-Sr-s as measured by the GOES satellites (http://umbra.nascom.nasa.gov/SEP/). This filtering was necessary, because solar proton events can inject very large numbers of protons into the magnetosphere, independent of the processes that SAAMAPS is designed to model. Including solar proton events would introduce statistical anomalies into the dataset, reducing the accuracy of the model.

One additional observation about the T7 channel is important. Unlike the other proton response channels, T7 is an anti-coincidence channel (D. Bronek, private communications, 2006). This means that T7 only collects information from the back detector (DBT). This makes T7 a useful channel in detecting high-energy protons capable of penetrating the copper walls of the telescope. It also means that T7 demonstrates a considerably wider field of view for these protons since protons are not limited to striking the top detector first. This played an important role in understanding the dependence of the observed anisotropy to proton energy ranges. Specifically, it explained why T7 results would sometimes appear to have considerably less anisotropy than what was expected for 40-200 MeV protons.

1.3.4. *Anomalous CEASE data*

After AFRL/VSBX sorted the CEASE data geographically and filtered for proton events, work began on analyzing the data for the development of the SAAMAPS model. This work was impeded by an unanticipated result in the CEASE data. Figure 1.6 shows a histogram of all the protons in the T6 energy channel that CEASE observed in the 27°-30° south latitude, 315°-318° longitude, and 1000-1050 km altitude bin. If the proton flux measured in this bin was experiencing just random variations, than the histogram should show a Gaussian distribution peaked near the average value for the bin.

Instead, Figure 1.6 shows a bi-modal distribution with very few measurements occurring near the average value. Additionally, a significant number of measurements were observed outside of the standard deviations. While isolated cases of such behavior could be statistically accounted for, the bi-modal histograms were found in numerous bins across a range of altitudes, latitudes, longitudes, and across the energy channels that were measured. Since the proposed model will make use of average flux values and the standard deviations, it is necessary to account for what is causing the bi-modal distributions, so that the data can be adjusted accordingly.
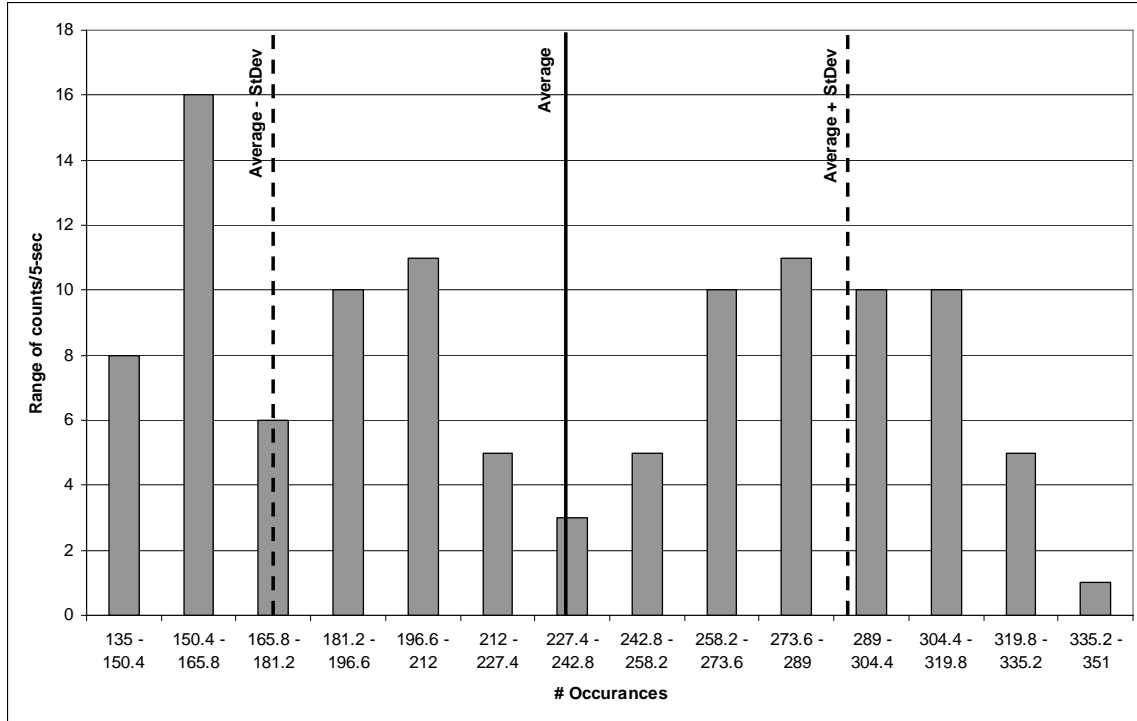
Figure 1.6: Histogram of >25MeV proton counts in the -30°, Lat, 315° Long, 1000km Alt bin showing a bi-modal distribution pattern

In trying to understand the cause of the problem, the scientists at AFRL/VSBX recast the data in a new format. Figure 1.7 displays the same data as Figure 1.6, but this time the flux measurements are plotted as a function of the measurement date. Additionally, the data is broken up into subsets based upon whether TSX-5 was traveling generally southward or northward through the bin at the time of measurement. With the exception of the final few satellite passes (which were not yet available when this theory was initially proposed), the northern traveling and southern traveling data sets appear to separate into two regimes – upper and lower, roughly separated by 2.25×10^2 counts/5-sec. Scientists at AFRL including Greg Ginet, Bronek Dichter, Donald Brautigam, and Dan Madden, theorized that the direction of travel was leading to the bi-modal nature of the histograms. Further analysis revealed that CEASE was mounted such that it looked 90° off of TSX-5's direction of motion. This would result in the satellite taking measurements looking eastward or westward depending on the direction of travel through the bin.

From this information, the scientists developed the hypothesis that the dual-peaked nature of the histograms was the result of a phenomenon known as the East-West Effect. The purpose of this research was to test that hypothesis.
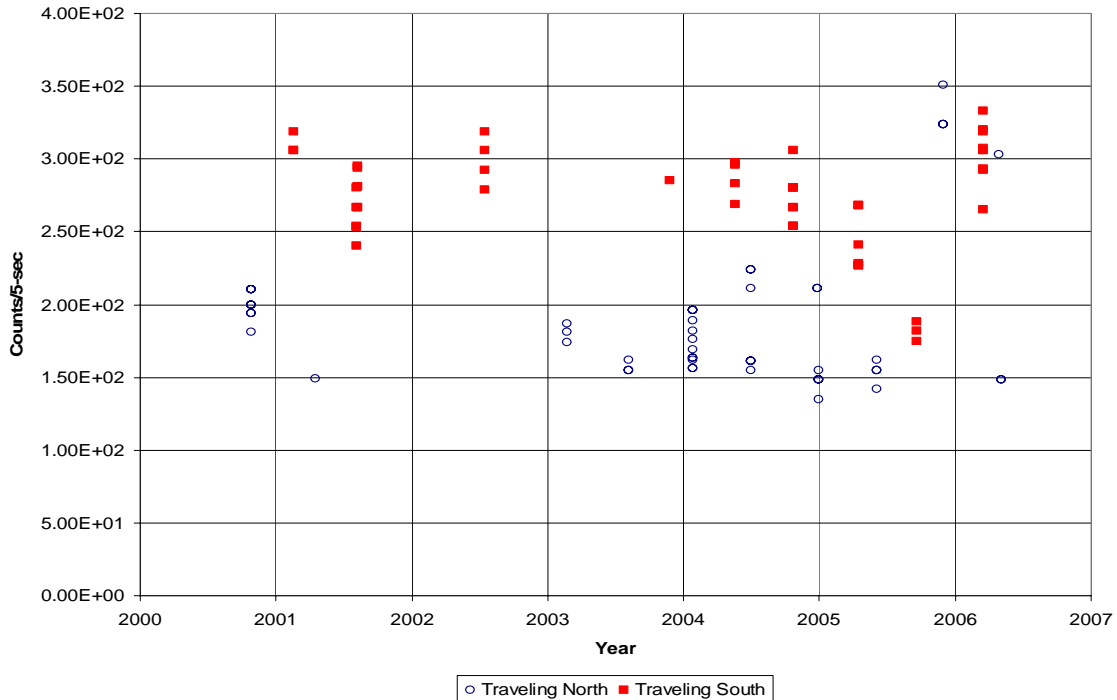
Figure 1.7: Chronological occurrence of >25 MeV proton counts in the -30° Lat, 315° Long, 1000km Alt bin showing northward and southward traveling passes (G. Ginet, private communication, 2006)

1.3.5. *The East-West Effect*

The East-West Effect describes a well-documented anisotropic behavior in the South Atlantic Anomaly. First proposed by *Lenchek and Singer* [1962], the East-West Effect describes how protons undergoing gyro-motion around magnetic field lines can lead to fluxes displaying a strong eastward bias. This is in accordance with the first adiabatic invariant which states that charged particles will maintain a constant magnetic flux inside their radius of gyration about a magnetic field line. The radius of this rotation is dependant on the charge of the particle, q, the particle's velocity, $v_{\perp}$, the particle's mass, m_p, and the strength of the magnetic field, B, as seen in

14

Equation 1.1. Typically, particles are described in terms of their energies, so it is necessary to

convert the energy to a velocity. This is shown in Equation 1.2 for non-relativistic particles.

$$r_g = \frac{m_p \cdot v_\perp}{|q| \cdot B}$$

(1.1)

$$v = \sqrt{\frac{2E}{m_p}}$$

(1.2)

An additional observation is that the direction of rotation is dependent on the charge,

meaning that all protons will orbit about field lines in the same direction (counter-clockwise when

looking toward magnetic north).
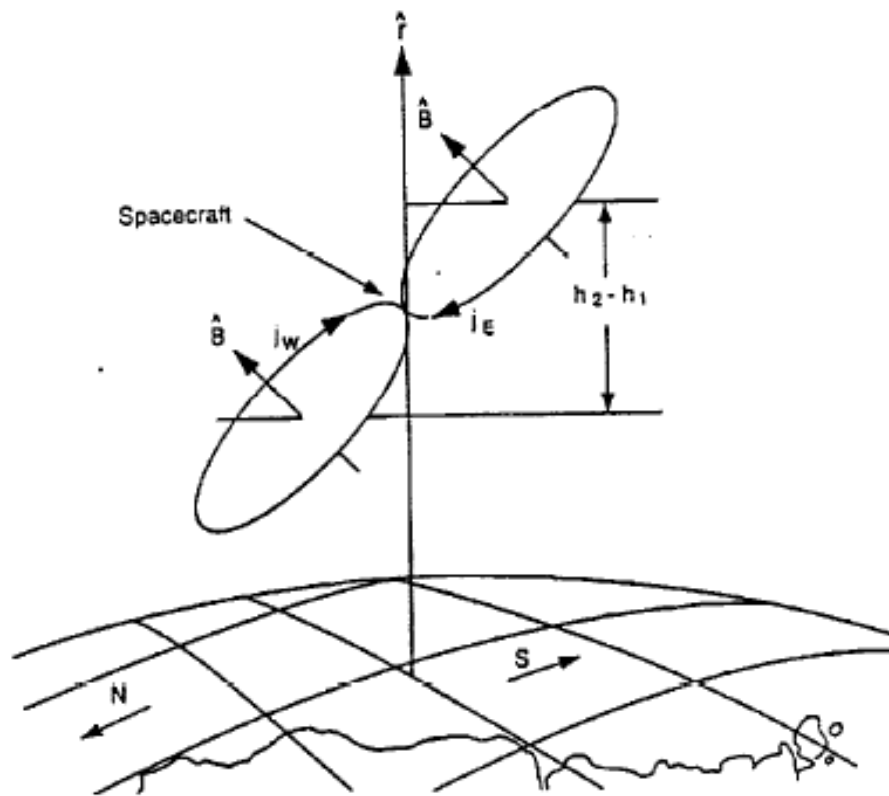
**Figure 1.8: Depiction of the East-West Effect caused by protons following gyro-radii above
and below an observation point "spacecraft" [*Armstrong et al.*, 1990]**

Figure 1.8 depicts the effect that this directional gyro-motion has upon a fixed point in

space. At the point, labeled "spacecraft" in the figure, protons are coming from two different

15

directions, east and west. The flux represented by j_E is traveling eastward at the reference point and is orbiting a field line at a higher altitude. The flux represented by j_w is traveling westward at the reference point and is orbiting a field line at a lower altitude.

This becomes important, because the gyro-radii are large enough to observe changes in atmospheric density between the upper and lower loops. Specifically, protons in the upper loop will be traveling through a thinner atmosphere than protons in the lower loop. This will lead to different collisional loss rates, where the flux of protons traveling eastward will be greater than the flux of protons traveling westward. This effect is described in greater detail in Appendix A, which includes an example of sample proton fluxes within the SAA.

Lenchek and Singer [1962] were able to characterize this behavior by making use of several simple formulas. First, they observed that the probability p of a proton to be detected by at the observation point is inversely proportional to the atmospheric density ρ that the proton traveled through, as shown in Equation 1.3. For instance, if the atmospheric density increases, there is an increased likelihood of a collision, resulting in a lower probability of detecting a proton.

$$ p \propto \frac{1}{\rho} \tag{1.3} $$

Because of the size of the gyro-radii, the atmospheric density that the lower loop travels through will not be the same as the atmospheric density the upper loop travels through. If the size of the gyro-radii is significantly less than the scale height, h, than a simplifying assumption can be made. For a<<h, the atmospheric density at the center of the gyro-radius will be used as the average atmospheric density over the entire loop. This assumption does not work for cases when a approaches the size of h, however. In these cases, the proton would actually travel through a significant range of atmospheric densities causing the atmospheric density at the center of the orbit to not accurately reflect the average atmospheric density.

If the angle between the magnetic field vector and the vector normal to the Earth's surface is known, it becomes possible to calculate the atmospheric density for the two gyro-radii centers. Figure 1.9 depicts this angle as θ, which is synonymous with the dip angle, I.
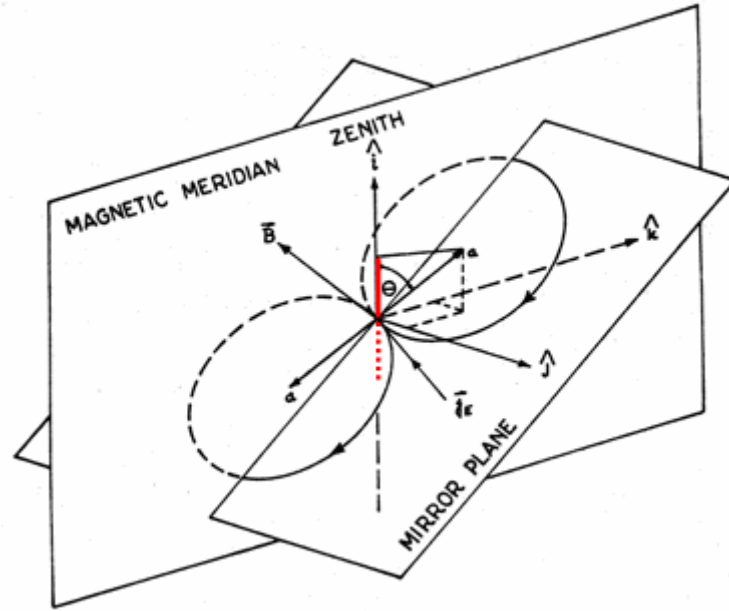
Figure 1.9: Geometry showing the difference in altitude between the centers of the gyro-radii corresponding to the eastward and westward fluxes [*Heckman et al.*, 1963]

If we assume a logarithmic atmosphere, than the atmospheric density at any altitude can be described by Equation 1.4, where $\rho(z_0)$ is the atmospheric density at some reference altitude, z_0, and h is the scale height. An examination of Figure 1.9 reveals that the z for the eastward flux loop and westward flux loop can be expressed by Equations 1.5a and 1.5b.

$$\rho(z) = \rho(z_0) \cdot \text{Exp}\left[\frac{z - z_0}{h}\right] \qquad (1.4)$$

$$z_e = z_0 + a \cdot \cos[I] \qquad (1.5a)$$

$$z_w = z_0 - a \cdot \cos[I] \qquad (1.5b)$$

Combining Equations 1.3, 1.4, and 1.5a&b yields an expression (Equation 1.6) for the probability of measuring protons from either the eastward or westward flux.

$$p(z_0, \tfrac{E}{W}) \propto \left[\rho(z_0) \cdot \mathrm{Exp}[\tfrac{\mp a \cdot \cos(I)}{h}] \right]^{-1} \tag{1.6}$$

Since the observation point is experiencing both eastward and westward fluxes it is useful to compare the two probabilities as a ratio. This ratio is given as j_e/j_w, and takes the form seen in Equation 1.7. This is nearly identical to the equation proposed in Lenchek & Singer [1962], except that the angle they used has been updated to the dip angle, I, in accordance with modern convention.

$$j_e/j_w = \exp\left[\frac{2a \cdot \cos[I]}{h} \right] \tag{1.7}$$

In Lenchek and Singer's paper, they used an approximation for the scale height values. Today, the scale height used in the equation can be derived from the neutral atmosphere Mass Spectrometer Incoherent Scatter (MSIS) model. MSIS calculates various atmospheric number densities and temperatures for a given point and time. From the number densities, the average mass can be calculated by multiplying the mass of each particle by its MSIS-derived number densities, summing those masses together, and dividing by the total number density. These average masses and the MSIS-calculated temperatures can be entered into equation 1.8, to derive the scale height. An analysis of this equation reveals that at higher altitudes, the scale height increases, meaning that the atmospheric density differences between the upper and lower orbits will gradually diminish.

$$h = \frac{k_B T}{\langle m \rangle g} \tag{1.8}$$

The gyro radius needed in Equation 1.7 is given by Equation 1.9 as a function of proton mass, m_p, the charge of a proton, q_p, magnetic field strength encountered by the proton, B, and the tangential velocity of the proton $v_\perp$. The magnetic field strength can be derived from another model called the International Geomagnetic Reference Field (IGRF), which calculates the

magnetic field strength for a given point and time based upon a series of spherical harmonics determined by careful observations of the Earth's magnetic field. The velocity of each particle was previously shown in Equation 1.2.

$$a = \frac{m_p \cdot v_\perp}{q_p \cdot B}$$

(1.9)
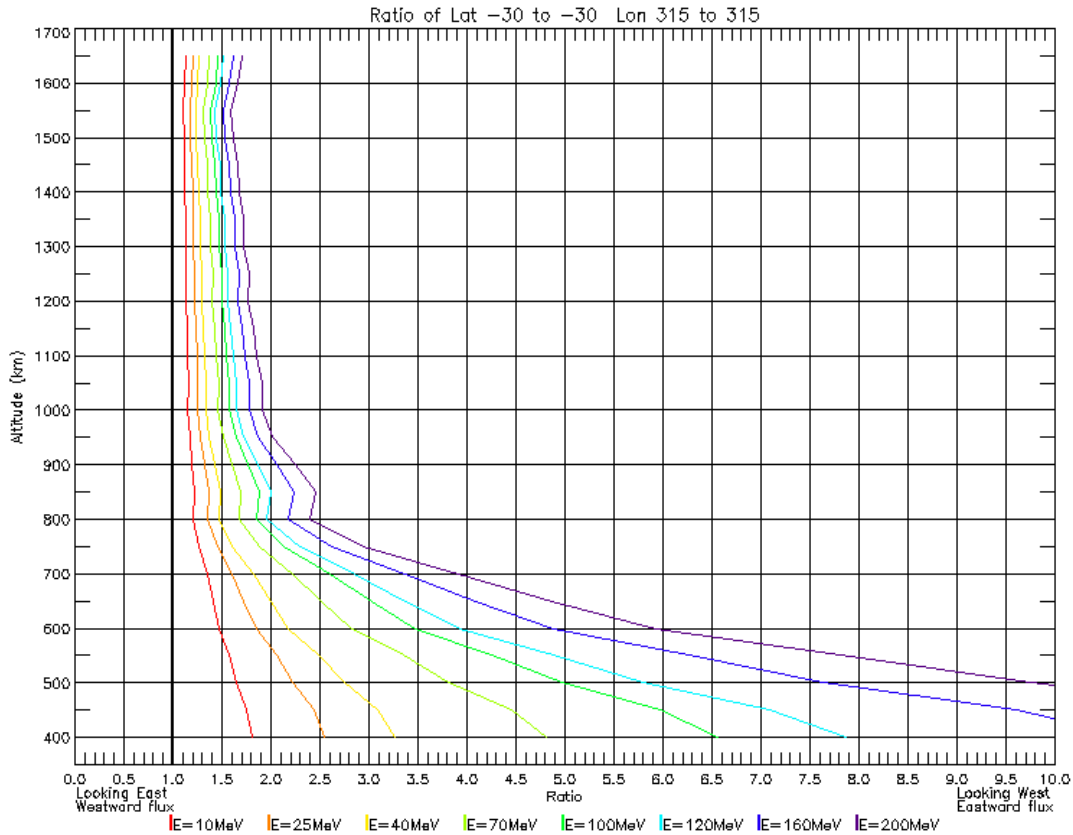
Figure 1.10: Altitide-dependent east-west ratio curves for various proton energies at the point 30ºS, 315ºE

Given all of this information, it is possible to construct plots of how the east-west ratio is affected by its various components. For example, Figure 1.10 is a plot of 8 different east-west ratio curves, showing the dependence of the curves to altitude and proton energy. The energy of the proton being studied is very important, because it determines the size of the gyro-radii. Higher energy protons, such as 100 MeV, will have larger gyro-radii taking them lower or higher

in the atmosphere, leading to larger differences between the two orbits' average atmospheric density. This, in turn, amplifies the difference in the collisional loss rates for the two fluxes, leading to an increase in the east-west ratio, as seen in Figure 1.10.

It should be pointed out that the higher energy curves shown in Figure 1.10 are based strictly on Equation 1.7 and don't take into account the assumption stated above. Because of the large scale heights of the upper atmosphere, at higher altitudes, these curves would be correct. At lower altitudes, however, the curves may not accurately represent the east-west ratios that would actually be encountered. Figure 1.10 also demonstrates the altitude-dependent behavior of the east-west ratio. At low altitudes, a dominant eastward flux is expected, because the vertical differences in atmospheric density are highest at that altitude, leading to significant differences in the collisional loss rates. As altitude increases, the atmospheric difference between the two gyro-radii gradually diminishes resulting in converging collisional loss rates and an east-west ratio approaching 1.0 for all energy channels.

Work on the East-West Effect extends beyond theory. Since its discovery, the East-West Effect has been well studied at the altitudes of the space stations and space shuttles (~300-400 km altitude). Examples include results from Mir [*Badhwar et al.*, 2002], the International Space Station [*Dachev et al.*, 2006], and the space shuttle [*Sakaguchi et al.*, 1997]. Results have strongly supported the theories laid out by Lenchek and Singer.

An interesting problem results in trying to apply the East-West Effect to the results seen in Figure 1.7. Figure 1.10 shows that a 25 MeV proton flux at 1000km altitude should have an east-west ratio of ~1.25. In reality, this data corresponds to an east-west ratio of 0.697, a result that could not be explained by the East-West Effect at all. But, while the east-west effect did not play a significant role in the bin studied in Figure 1.7, it was found to have an important role in other bins throughout the SAA, a result which will be discussed in Section 3.3. For the bin in

question, the east-west ratio was found to actually be the result of pitch angle differences between when TSX-5 was traveling north vs. when it was traveling south through the SAA.

1.3.6. Pitch angles and their impact on the data

A particle's pitch angle is the angle between a particle's velocity vector and the magnetic field line that it is orbiting [*Rees*, 1989]. A pitch angle close to 0° or 180° implies that the particle is traveling close to parallel to the magnetic field line. As the particles get further north or south, the magnetic field lines come closer together, increasing the magnetic flux density. This results in a force which decreases the northward or southward component of the particles' velocities, changing the particle's pitch angle. When the particle's pitch angle reaches 90°, the particle is orbiting the magnetic field with no component parallel to the magnetic field at all. This is usually a temporary state because the forces that slowed the particle down are continuing to act, causing the particle to reverse its trajectory. This results in a "bounce motion" consistent with the second adiabatic invariant of plasma physics [*Sturrock*, 1994]

Some particles are able to avoid this bounce motion. Particles at or near a pitch angle of 0° or 180° are in the "loss cone" meaning that they are not trapped magnetically and have a sufficient parallel velocity to escape into the Earth's atmosphere [*Sturrock*, 1994]. Pprotons at pitch angles near the loss cone will occasionally be bumped into the loss cone, resulting in a diffusion effect. In the case of a symmetric magnetic mirror, pitch angle diffusion occurs equally near both loss cones, meaning that the point of maximum particle population will occur at 90 degrees.

This is demonstrated in Figure 1.11, which plots the proton population as a function of pitch angles. It shows that at any given latitude, the largest number of particles will be traveling at a pitch angle of 90°. Based upon this figure, the optimal orientation for a satellite's proton detector to measure proton flux is for the detector to be oriented 90° from the Earth's magnetic

21

field lines. This angle can be called the satellite's look angle. If the pitch angle is not close to

90°, the satellite may not be able to measure protons traveling at a pitch angle of 90°, resulting in

a lower count. Instead, the detector would only be able to sample from a reduced flux at

whatever pitch angle it happens to be looking at.
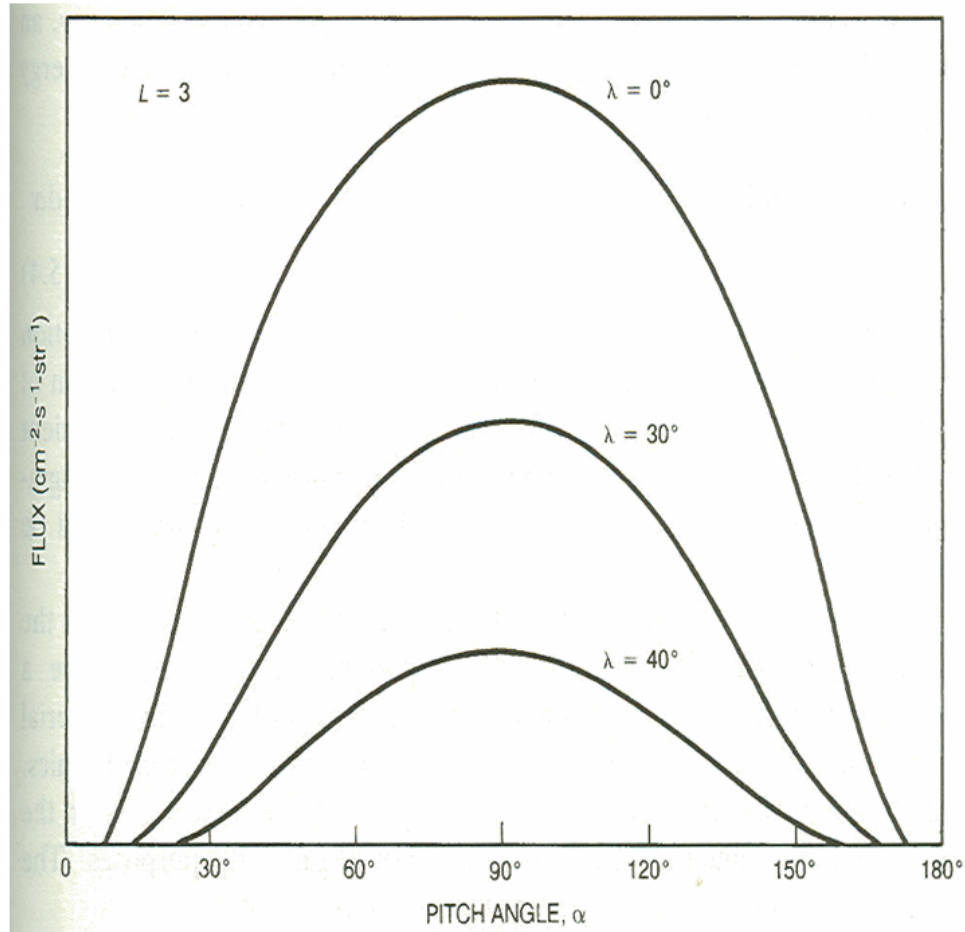
Figure 1.11: Flux distribution across pitch angles for three latitudes, λ, taken at the L=3 L-shell, [Walt, 1994]

Normally, sampling from a reduced flux would have no bearing on measurements of the

East-West Effect. Equation 1.7 shows that the east-west ratio has no dependence on the protons'

pitch angles. In fact, the pitch angle distribution shown in Figure 1.11 would affect both the

eastward and westward fluxes nearly identically (a negligible widening of the eastward

distribution would occur because of the increased altitude of the eastward flux).

However if the eastward and westward measurements were taken at different satellite pitch angles, a potential measurement bias could be introduced. For instance, consider the flux of the $\lambda=30^o$ curve in Figure 1.11. If one measurement was taken at a pitch angle of 90°, it would have the maximum particle population from which to make its measurement. If the other measurement was taken at a pitch angle of 60°, however, there would be fewer protons available to measure, resulting in an artificially lowered measurement. This would lead to an adjusted east-west ratio, unless some way could be found to account for the changes introduced as a result of the measurement bias. In fact, such a measurement bias was discovered within the CEASE data set and it did have impacts upon many of the east-west ratios. This is discussed in greater detail in Section 3.2.

1.3.7. *Solar Cycle Variability of the East-West Effect*

In AFRL/VSBX's treatment of the CEASE data, they have thus far chosen to neglect the impacts of solar cycle variability upon the data. When the scientists first started analyzing the data, TSX-5 had only experienced solar maximum conditions, and was not expected to survive until solar minimum. However, the satellite did survive until very close to solar minimum, giving them an opportunity to analyze solar cycle variability.

The solar cycle is important, because the density of the atmosphere varies in response to the amount of solar input. During solar maximum, the sun releases more energy at shorter wavelengths than at solar minimum. This increased energy is transferred to atmospheric neutral particles as kinetic energy, which allows them to travel higher in the atmosphere. As a result of this, atmospheric densities increase between solar minimum and solar maximum.

Equation 1.3 showed that the probability of measuring a particle is inversely proportional to the atmospheric density. Since atmospheric density is higher at solar maximum, there is an

increased likelihood of measuring particles at solar minimum, because the number of proton-neutral collisions is reduced. This means that proton fluxes in the SAA will be higher during solar minimum than solar maximum.

Less obvious is the impact that this will have upon anisotropy. Increased temperatures at solar max will increase scale heights. Equation 1.7 reveals that an increase in scale heights should serve to lower the east-west ratio. Thus, the east-west ratio should be higher at solar minimum than solar maximum.

As an example, Table 1.2 shows how the atmospheric density and temperature of neutral particles at a given point (50° Lat, 210° Long, 400 km alt) changes in response to the solar cycle. Specifically, the atmospheric density increased nearly 400% between solar minimum and solar maximum. This was accompanied by a ~250K rise in temperature over the same time.

Table 1.2: Dependence of atmospheric density at 50° Lat, 210° Long, 400 km altitude to variations in F10 and F10A which vary in response to the solar cycle [Rees, 1989]

	F10	F10A	Atmospheric Density (g/cm^3)	Neutral Temp (K)
Solar Minimum	74.5	86.1	2.687×10^{-15}	1043
Solar Maximum	243.3	187.7	9.925×10^{-15}	1299

Also included are the F10 and F10A values contributing to these values. F10 is a measure of the sun's 10.7 cm radio flux on any given day and serves as a common proxy for solar activity. Likewise F10A is the 91-day average of F10 values centered about the day in question. In models that take solar activity into account (such as MSIS), it is common for the F10 and F10A values to be used to describe the amount of solar input.

In neglecting solar cycle variability, it's possible that variations may exist in the data set outside of those caused by strictly random behavior. In fact, several factors were observed that indicated this may be occurring. These factors are presented in Section I.3.5.

II. Procedures and Resources

2.1. Procedures

2.1.1. Data Preparation

The first step in analyzing the data from the CEASE instrument was to resort the data from a chronological arrangement into the 3° latitude by 3° longitude by 50 km altitude bins better suited for an analysis of geographic regions such as the South Atlantic Anomaly. This resolution was chosen to conform to the work AFRL/VSBX had already conducted. Furthermore, this research also conformed to the nomenclature that AFRL/VSBX had established in referring to each bin. Each bin is identified by the latitude (in degrees north or south) and longitude (in degrees east) corresponding to the bin's southwest corner. The bins are also sorted by altitude such that all measurements ≥400 km and <450 km are sorted into one altitude directory corresponding to the lower altitude limit (e.g.: 0400). All future references to geodetic bins throughout this report make use of this naming convention.

Because of the nature of TSX-5's orbit and the size of the bins, the measurements in each geodetic file are not uniformly spread throughout the mission span of the satellite. Instead, measurements are often grouped in time representing individual satellite passes through a given geodetic bin. The result is that a given bin might contain 10 consecutive measurements, representing a 50 second span of data, only to be followed by a months long gap with no measurements at all. An example of this can be seen in Table 2.1, which shows an excerpt from one of the geodetically-sorted data files. It shows a series of 5 measurements taken on 14 June 2000, followed by 8 measurements taken just 7 days later. The next set of measurements isn't until 5 Jan 2001, 198 days later. No measurements were taken for this bin during that 198 day period, because TSX-5 did not pass through this bin over that time span. This chronological bunching effect had important impacts on the statistics used in analyzing the data, as seen in

Section 3.5.

Table 2.1: Excerpt from the -30°S, 315°E, 400 km altitude data bin demonstrating the chronological bunching of measurements caused by satellite passes through the bin

Year	Day	UTSec	Geodetic Altitude	Geodetic Latitude	Longitude
2000	166	31307	422.4	28.6	315.04
2000	166	31312	423	28.91	315.18
2000	166	31317	423.6	29.22	315.31
2000	166	31322	424.3	29.53	315.45
2000	166	31327	425.2	29.83	315.59
2000	173	25979	435.4	27.55	315.1
2000	173	25984	436.4	27.85	315.24
2000	173	25989	437.6	28.16	315.37
2000	173	25994	438.7	28.47	315.51
2000	173	25999	439.8	28.77	315.65
2000	173	26004	440.9	29.08	315.79
2000	173	26009	442.1	29.38	315.92
2000	173	26014	443.2	29.69	316.06
2001	5	1370	435.6	29.73	317.5
2001	5	1375	434.6	29.43	317.64
2001	5	1380	433.5	29.12	317.78
2001	5	1385	432.7	28.82	317.92
2001	7	527	429	29.21	315.07

2.1.2.   East vs. West Analysis

In testing the East-West Effect hypothesis laid out in Section 2.1.2, the next step was to associate each measurement with the instrument look direction. To describe this, a clearer understanding of the coordinate system used in the ephemeris data set is needed.

Each measurement consisted of four vectors: the CEASE instrument look vector ($\vec{O}$), the direction of the magnetic flux taken from the combination of IGRF and an external magnetic field model called Tsygenenko ($\vec{B}$), the position of the TSX-5 satellite ($\vec{d}$), and the velocity of the satellite ($\vec{V}$). All four vectors were given as x, y, and z components in the Earth-Centered Inertial (ECI) coordinate system. This coordinate system is defined by an x-axis pointing in the direction of the sun at vernal equinox, a z-axis parallel to the Earth's rotational axis and pointing northward, and a y-axis orthogonal to both x and z forming a right-handed coordinate system.

Figure 2.1 shows the ECI-based axes with the Earth shown for reference.
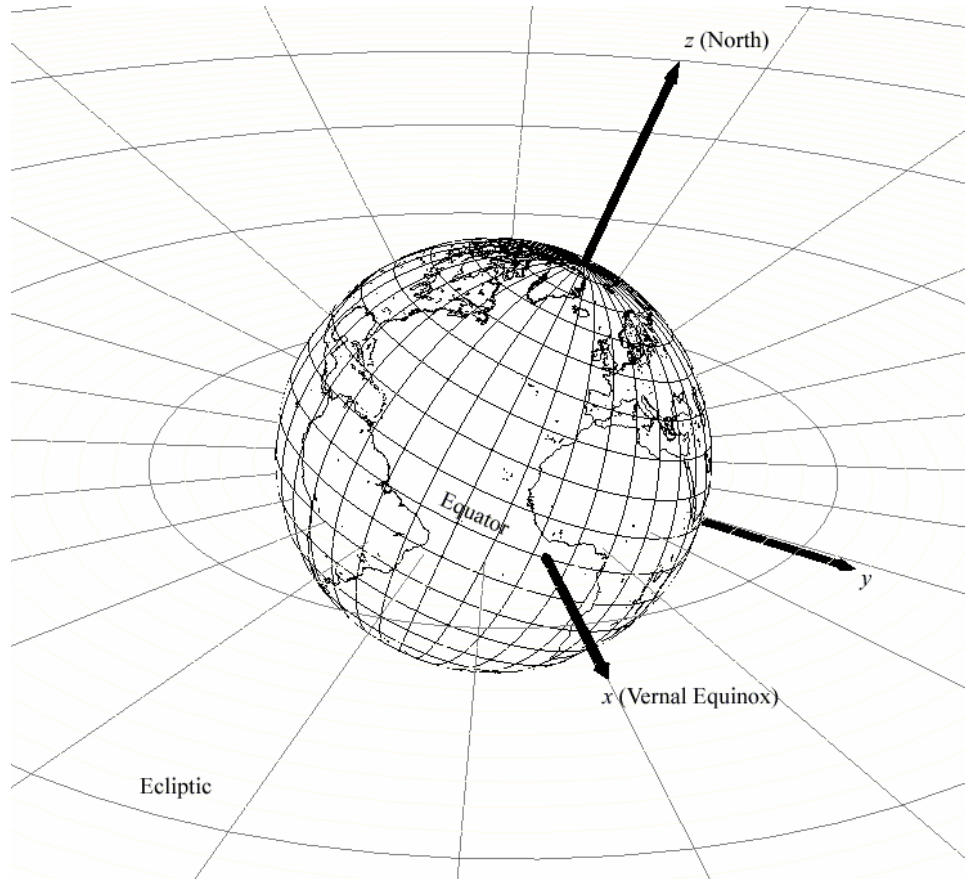
Figure 2.1: Graphical depiction of ECI coordinate system with Earth shown for reference
(http://www.celestrak.com/columns/v02n01/)

From this information it is possible to construct a satellite-centered geomagnetic

reference basis that will facilitate the determination of CEASE's relative look direction.

Appendix B describes this process in detail making use of a sample measurement from the data

set as an example. The basic geometry, as shown in Figure 2.2 is to take the satellite-centered

reference frame which uses $\vec{P}$ and $\vec{B}$ to derive the direction of magnetic west, $\vec{W}$ and a vector, $\vec{Q}$

orthogonal to both $\vec{B}$ and $\vec{W}$. Projecting satellite-centric vectors onto the QW plane allows an

angle θ to be calculated clocked from vector $\vec{Q}$ such that $0 < \theta < \pi$ indicates a westward-

pointing vector and $\pi < \theta < 2\pi$ indicates an eastward-pointing vector.
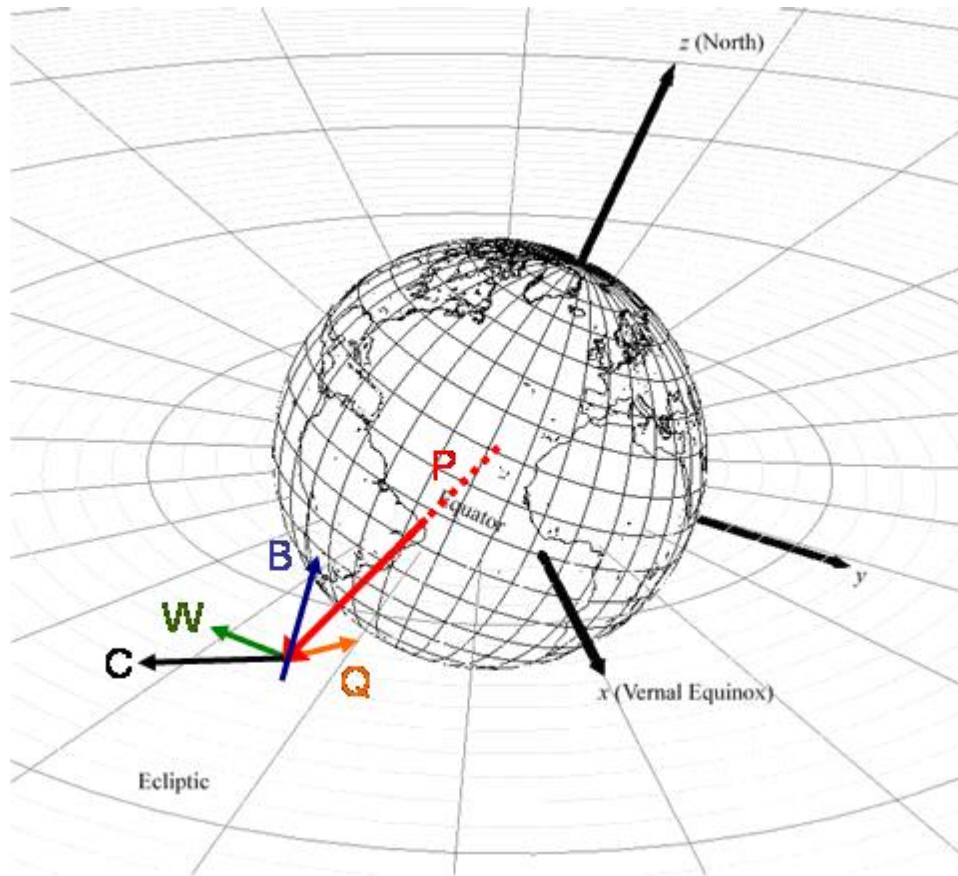
Figure 2.2: Depiction of coordinate system and vectors used to determine clock angle

When this technique is applied to the CEASE look vector, $\vec{C}$, it becomes possible to

determine whether the instrument is looking east or west relative to the magnetic field line.

However, when the instrument is looking west, it is actually measuring particles traveling

eastward, and vice versa. Since the East-West Effect predicts a higher eastward traveling proton

flux, a higher flux should be expected when the instrument is pointed towards the west. To

reduce confusion on this point, a consistent nomenclature was chosen such that look directions

are written as west- or east-looking, while proton fluxes are east*ward* or west*ward* traveling. This

convention is used throughout this thesis.

Using the clock angle technique, the dosimeter/telescope and ephemeris data sets were

merged into a unified geodetically-binned data set that included clock angle information. Also

included in the files was information on whether the measurement was taken during a solar proton event.

Each file in the merged data set corresponded to a geodetic bin (3° latitude x 3° longitude x 50km alt). Each file was run through an IDL program that averaged all the non-proton event west-looking measurements and east-looking particle counts.

The two averages were compared by taking the ratio of the west-looking measurements (eastward flux) over the east-looking measurements (westward flux). This ratio is useful in that any ratios greater than 1.0 suggest the presence of the East-West Effect, while ratios less than 1.0 suggest a predominantly westward flux, and some other process.

2.1.3.   Uncertainty and Error Propagation

In analyzing the east and west ratios it is important to realize that the measured average may not accurately reflect the actual average of proton counts in that region. This can be the result of observations that do not accurately reflect the proton population at that instance. Alternately, it might be because the observations used to compute the average are being skewed by a limited selection of data points. Using too few (or an unfortunate selection) of data points can cause problems because the actual number of protons in the region changes as a result of random processes within the magnetosphere. Taking certain measurements a few hours later could lead to minor differences of the measured average.

This situation leads to the consideration of uncertainty in the flux calculations and the resulting ratios. In this case, the uncertainty estimates the likelihood that the measured average counts (as calculated in Section 2.1.2) is not the actual average, but significantly close to it. In order to account for this discrepancy, counts are reported as the measured average value ± a range of values around it, such that the actual count value should fall somewhere within one of these ranges.

To estimate the ranges used for the measurements, uncertainty estimates were drawn

assuming a Poisson distribution. The Poisson distribution was selected because it "describes the

results of experiments in which we count events that occur at random but at a definite average

rate" [Taylor, 1997]. Appendix C explains the motivations for this assumption in more detail.

In short, the Poisson distribution states that the average uncertainty of the average east or

west flux is the square root of the total number of counts, Σn, divided by the number of

measurements, i, used to draw the average (see Equations 2.1 a & b).

$$\sigma_e = \frac{\sqrt{\sum n_e}}{i_e} \qquad (2.1a)$$

$$\sigma_w = \frac{\sqrt{\sum n_w}}{i_w} \qquad (2.1b)$$

The application of this technique made use of a FORTRAN routine to scan each file line

by line and determine from the derived clock angle whether the line corresponded to an east-

looking or west-looking measurement. Once the determination was made, a running sum of n_e

(east-looking) and n_w (west-looking) measurements for each channel was made while also

counting the number of east and west measurements, i_e and i_w respectively. These values were

then used to calculate the average eastward or westward flux. Then the values were plugged into

an IDL routine of Equations 2.1a and 2.1b to compute the uncertainty of both averages.

Once the eastward and westward flux uncertainties were calculated it was necessary to

use error propagation techniques to derive the uncertainty of the east-west ratio. In this case, the

appropriate technique is addition in quadrature, since "the original uncertainties are independent

and random" [Taylor, 1997]. This is in large measure true for the CEASE data. Specifically the

formula to calculate the uncertainty of the east-west ratio using addition in quadrature is shown in

Equation 2.2. While this technique was applied to the entire CEASE data set, some data points

later in mission, as seen in Figure 1.7, were found to be anomalously high or low. This could

indicate some other physical process at work, instead of purely random variations, in which case,

accounting for them as uncertainties in a Poisson distribution would not be the correct method.

See Section I.3.5 for a more detailed treatment on this issue.

$$\sigma_{ratio} = \frac{j_e}{j_w} \sqrt{\left(\frac{\sqrt{\sum n_e}}{\sum n_e} \right)^2 + \left(\frac{\sqrt{\sum n_w}}{\sum n_w} \right)^2} \qquad (2.2)$$

Equation 2.2 was written into an IDL routine so that the uncertainty of each east-west

ratio for each energy channel could be plotted along with the ratios themselves. The results of a

sample calculation are provided in Appendix C.

2.1.4. *Geodetically Stacked Bins*

Once the east-west ratios and uncertainties have been constructed, it becomes possible to

analyze how any east-west anisotropy changes with respect to altitude. To accomplish this, the

26 ratios from a vertical stack of geodetic bins (e.g.: 30^oS, 315^oE, altitudes 400km – 1650 km)

were plotted using IDL. To facilitate plotting time, the routine was developed to allow any

combination of the energy channels T5 through T9 to be plotted simultaneously along with their

uncertainties.

The end result of this plotting algorithm would be a plot of east-west ratios by altitude for

some given bin, similar to the plot shown in Figure 1.10. Rather than depicting specific energy

levels, however, the results would plot whatever combination of channels T5-T9 the routine was

given as input conditions. Examples of these plots include Figures 3.2 -3.5 among others.

These plots were useful in that they provided a quick qualitative assessment of East-West

Effect behavior. This was accomplished by comparing the plotted results against the general

trend of the curves seen in Figure 1.10. Later, this style of plot would be repeated to plot

theoretical east-west ratios based upon the equations presented below.

2.1.5.   *Constructing a Theoretical Model*

After the east-west ratios were plotted, it was important to see if the results fit the

accepted theory on East-West Effect behavior. To accomplish this, a simple model was

constructed that calculated the theoretical east-west ratios for each measurement in the geodetic

bins. Because the experimental ratio is a complicated distribution of the energy spectrum

measured in each channel, it would be hard to recreate this with the theoretical ratio using a

simple model. However, it is possible to model a variety of discrete energy values and compare

them to the experimental results. The goal is to see if the model plots for the maximum and

minimum energies of any given channel bound the plot of that channel's east-west ratio as

derived from the experimental data.

Key to this theoretical model is Equation 1.6, which expressed the probability of

detecting a particle from the eastward or westward flux. In Section 1.3.5, the eastward and

westward flux forms of the equation were expressed in a simplified form. Then, a generic

atmospheric density, dip angle, and scale height were used in the equation to represent the stack

of bins at 30°S, 315°E. This method can be more precisely done to better match the results of the

TSX-5 measurements.

First, the measurements used to create the eastward and westward measurement averages

came from a discrete set of latitudes, longitudes, altitudes, and times. These specific parameters

can be used to construct an MSIS-derived atmospheric density and IGRF-derived magnetic field

for each measurement within the bin. Furthermore, the specific MSIS values can be used to

calculate what the scale height should be for that specific measurement, making use of Equation

1.8. The gyro-radius for each measurement can also be calculated, using Equation 1.9 and the

intensity of the magnetic field derived by IGRF. Like in Section 1.3.5, the energy values used to

compute the proton velocity were 10 MeV, 25 MeV, 40 MeV, 70 MeV, 100 MeV, 120 MeV, 160 MeV, and 200 MeV which corresponded to values considered by the T5-T9 data channels.

Once all of this information was assembled, the theoretical east-west ratio for each bin could be calculated. First, the clock angle was analyzed to determine if the derived atmospheric density, dip angle, scale height, and 8 gyro-radii corresponded to an east-looking or west-looking measurement. Then those values were input into the correct form (eastward or westward flux) of Equation 1.6. This would produce 8 different values, each describing the probability of measuring protons at one of eight different energies for a specific latitude, longitude, altitude, and time. This procedure was repeated for every measurement in the bin, making use of the correct form of Equation 1.6 each time.

After all of the probabilities were calculated, the eastward flux probabilities were added together and divided by the number of eastward measurements. The same was done for the westward flux probabilities. These probability averages were then divided as shown in Equation 2.3 to obtain the theoretical east-west ratio for that bin.

$$\frac{j_E}{j_W} = \frac{\langle p(r,E) \rangle}{\langle p(r,W) \rangle} = \frac{\sum p(r,E)/n_E}{\sum p(r,W)/n_W} \tag{2.3}$$

Once the ratio for each bin was known, these ratios were then run through plotting routines to compare the theoretical results to the actual measurements obtained by the CEASE satellite. For more on the comparison, please see Section 3.3.

2.2. Resources Required

The primary resource for this research was the CEASE data sets provided by AFRL/VSBX at Hanscom AFB. Between the ephemeris information detailing the TSX-5 position and the counts/5-sec data from the CEASE sensor, 14 GB worth of data was received.

The next resource was a workstation with sufficient computational power and data storage

capabilities to sort, store, and analyze the volume of data that had been received. While the computational power was easily available, data storage became an issue, because the files would need to be duplicated in a different format for them to be effectively used (see Section 2.1.1). Overall, over 52 GB of data was used in this research.

Additionally, FORTRAN 90 was chosen to program the data sorting routine, perform east/west determinations, and average the results of each bin. IDL 6.1 was then used to graph the results of the data, sometimes providing additional averaging or manipulation of the sorted data.

This research also made use of various space weather models currently available for general use. Specifically, the NRL Mass Spectrometer, Incoherent Scatter Radar Extended Model (NRLMSISE-00), shortened to MSIS, was used to calculate the concentration of neutral particles in the atmosphere under specific conditions. The program also calculated temperatures necessary for the scale height equation. The model accomplishes this through the use of "low-order spherical harmonics… to describe the major variations through out the atmosphere including latitude, annual, semiannual, and simplified local time and longitude variations" (http://uap-www.nrl.navy.mil/models_web/msis/msis_home.htm). This model represents an updating of work originally compiled in papers by A.E. Hedin [1983, 1987, 1991].

The second model used throughout this research is IGRF-10. IGRF is a model of the Earth's geomagnetic field made available by the International Association of Geomagnetism and Aeronomy (http://www.ngdc.noaa.gov/IAGA/vmod/igrf.html). The model describes the Earth's magnetic field making use of 13 orders of spherical harmonics. The data used to construct the model is assembled from various ground stations across the Earth and satellites in Earth orbit. To account for secular changes in the Earth's magnetic field, updates to the model are made available every 5 years, with the most recent update (IGRF-10) occurring in 2005. Values of the magnetic field for measurements taken in 2006, make use of a extrapolation routine carried within the model.

Both the MSIS and IGRF models are freely available in several formats. In this case, they were run as FORTRAN subroutines within the theoretical modeling program described in Section 2.1.5.

III. Results & Analysis

3.1. Confirmation of an East-West Anisotropy

The first goal of the research was to verify whether the observed bi-modal distribution of particle was caused by the East-West Effect. As we will see, at low altitudes the data supports this conclusion, while at higher altitudes a different process is at work.

By using the clock angle technique developed in Section 2.1.2, a new histogram of the -30° Lat, 315° Long, 1000 km Alt bin was constructed (Figure 3.1), this time sorting the data into eastward and westward fluxes. Assuming the East-West Effect is causing the double-peaked behavior, the sorted figure should demonstrate two overlapping Gaussian distributions, with the eastward flux corresponding to higher values, while the westward flux corresponds to lower values.
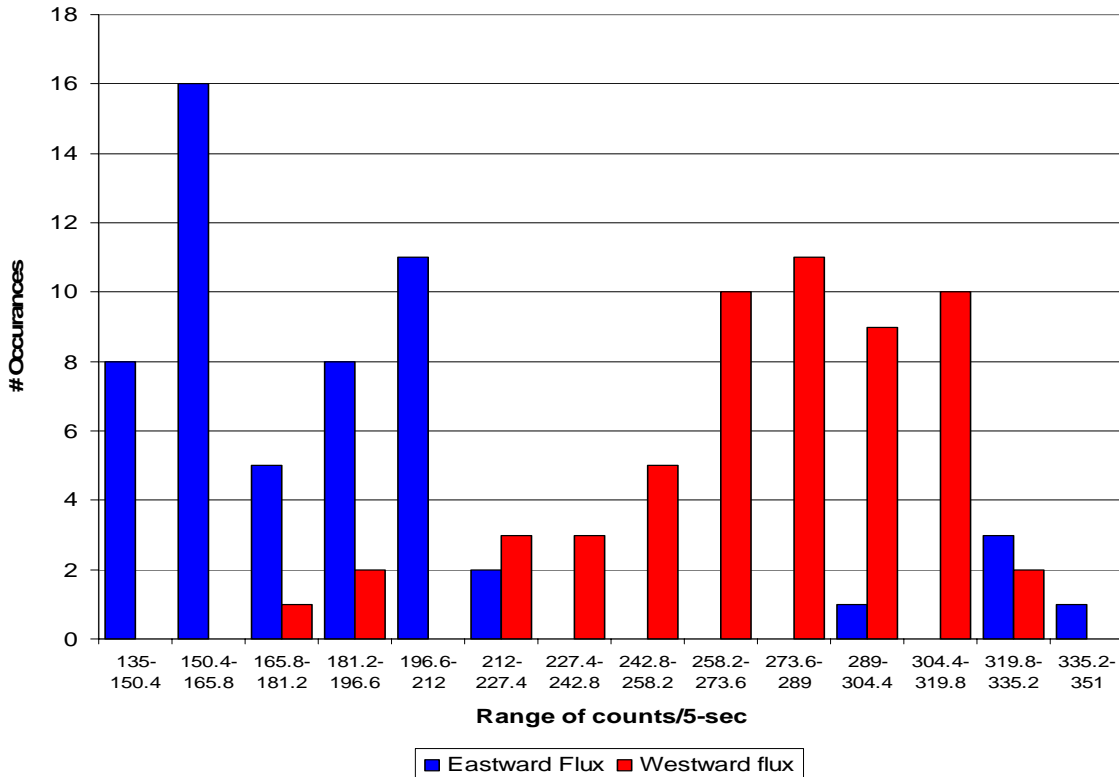
Figure 3.1: Histogram of >25MeV proton counts in the -30° Lat, 315° Long, 1000km Alt bin separated by Eastward and Westward fluxes

Calculating the east-west ratio for the bin confirms this fact. The ratio of the average eastward counts to the average westward counts is $j_e/j_w = 0.694 \pm .0085$, apparently indicating a significant dominance by the westward flux.
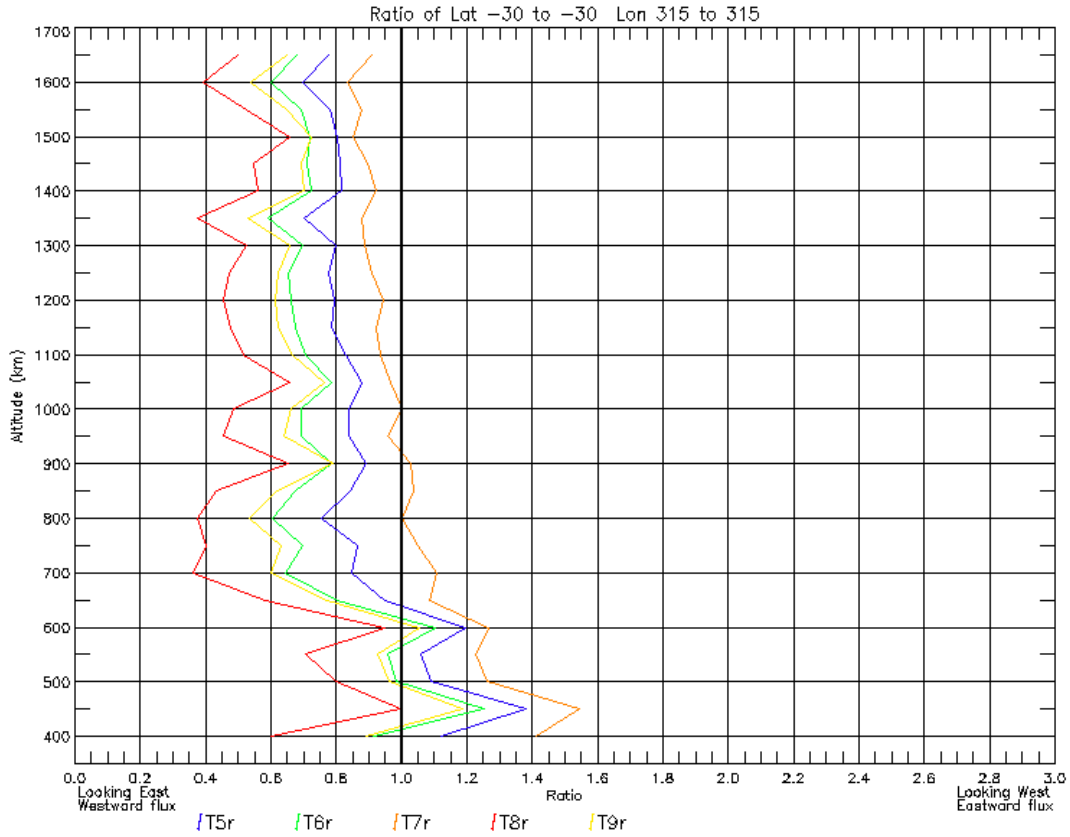
Figure 3.2: Plots of j_e/j_w ratios for energy channels T5 through T9 in the vertical stack of -30° Lat, 315° Long bins

To determine if this was an isolated incident, the east-west ratio for the -30° Lat, 315° Long bins at each altitude were plotted for energy channels T5 through T9. As seen in Figure 3.2, a significant number of the j_e/j_w ratios are less than 1.0, indicating general higher westward fluxes for that altitude and energy channel. Interestingly, at lower altitudes, several of the energy channels demonstrate the predicted behavior. Furthermore, the east-west ratios generally diminish with altitude, also in accordance with the East-West Effect theory. However, at high altitudes, no energy channel was observed to have a flux near or approaching 1.0. Instead, the

curves all depict a westward flux, not accounted for in the East-West Effect theory.

One early explanation for the dominant westward flux was that the calculated average values might lie within the error bounds of the anticipated East-West Effect. Section 2.1.3 described how the uncertainty of each average was calculated to define a range that the actual ratio would be within. Applying the error propagation technique to Figure 3.2, error bars have been added to the results of channels T7 and T8, the highest and lowest ratios respectively, at each altitude range. Figure 3.3 shows that the error bars are almost imperceptibly small. This implies that the anisotropy at high altitudes is not a product of random statistical errors.
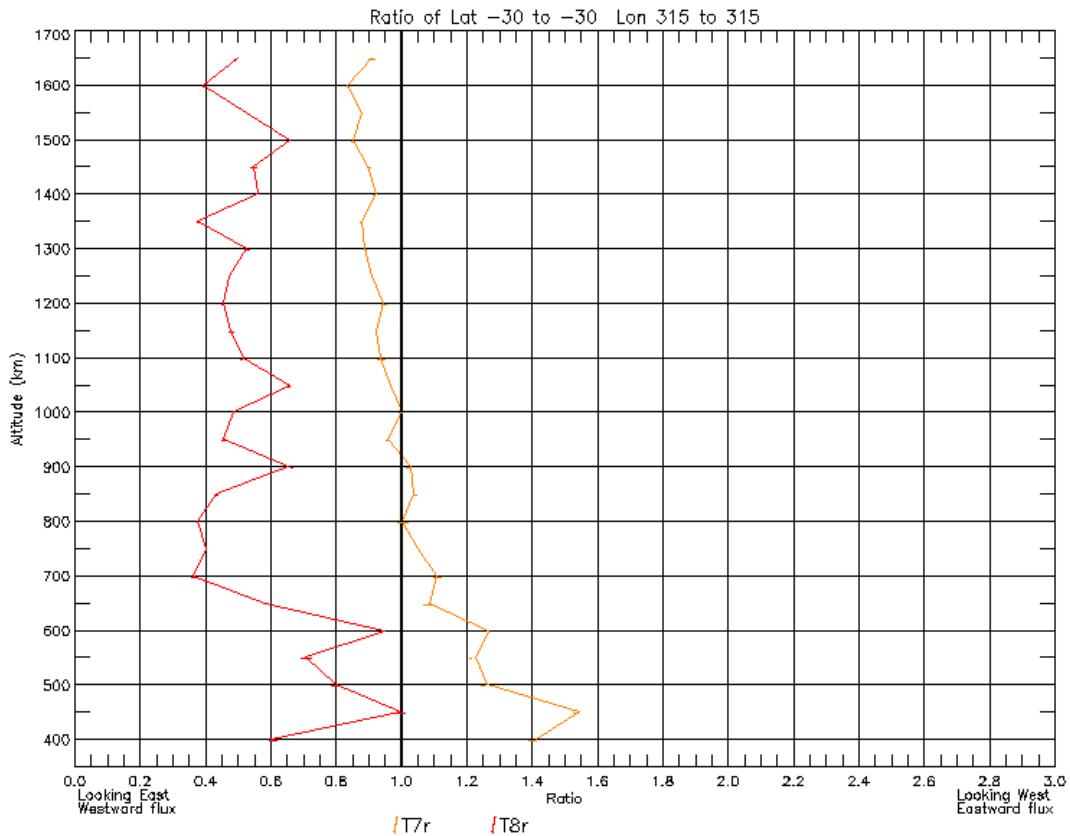
Figure 3.3: Plots of j_e/j_w ratios with error bars for energy channels T7 and T8 in the vertical stack of -30° Lat, 315° Long bins

3.2. The Effect of Pitch Angle Variability

An interesting feature of Figures 3.2 and 3.3 is how the ratios change as a function of altitude. In Figure 3.2, all the data lines show a larger west-east ratio at high altitudes than at low altitudes (400 to 650 km). As an example, the T8 energy channel goes from ~0.8 at low altitudes to ~0.4 at high altitudes. In the other data channels, the ratio exceeds 1.0 at low altitudes (excluding 400 km), gradually dissipating as altitude increases. This general trend supports the East-West Effect, but fails to describe what it causing the apparent offset at higher altitudes. The east-west ratios should be decaying to a value of 1.0, not 0.4 to 0.9, as is actually seen.

One possible explanation is that two physical processes are occurring, the East-West Effect, and a second effect resulting in westward offsets. Consider Figure 3.4 which plots the j_e/j_w ratios for the -6° Lat, 315° Long bins. In this case, the ratios clearly demonstrate the results expected by the East-West Effect.
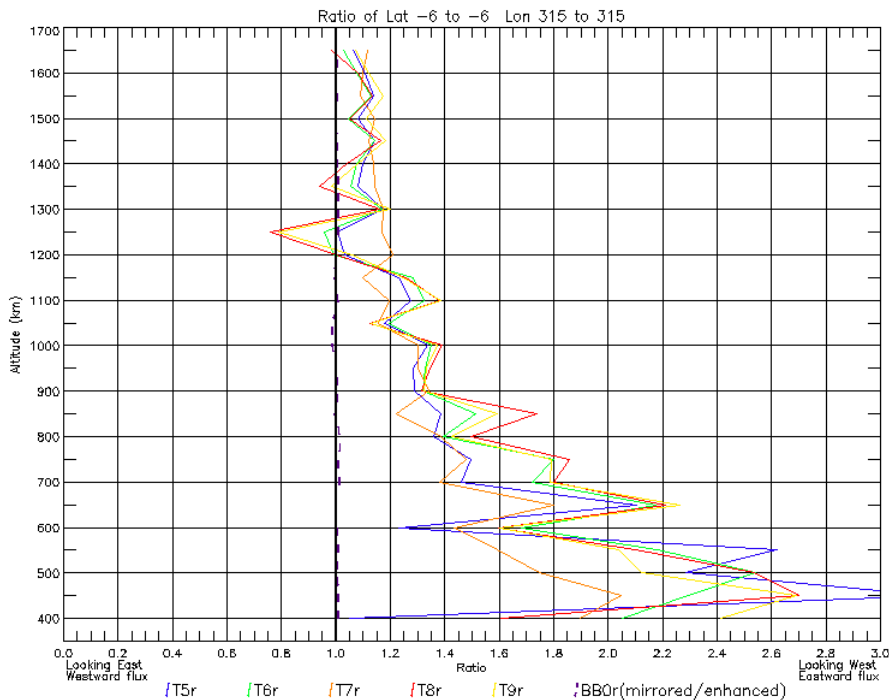
Figure 3.4: Plots of j_e/j_w ratios for energy channels T5 through T9 in the vertical stack of -6° Lat, 315° Long bins

In Figure 3.4 the five data channels demonstrate a similar and consistent decrease in the east-west ratio up to an altitude of ~1150 km, after which the ratio remains relatively stable at ~1.15. There appears to be no high-altitude offset in this plot making it appear as if the second physical process is not occurring.

Contrast this to Figure 3.5 which highlights the results from -45° Lat, 315° Long bins. In this case, there is a significant offset towards lower east-west ratios at all altitudes. This suggests that the second physical process is more dominant for this area, than in Figures 3.2 and 3.4.
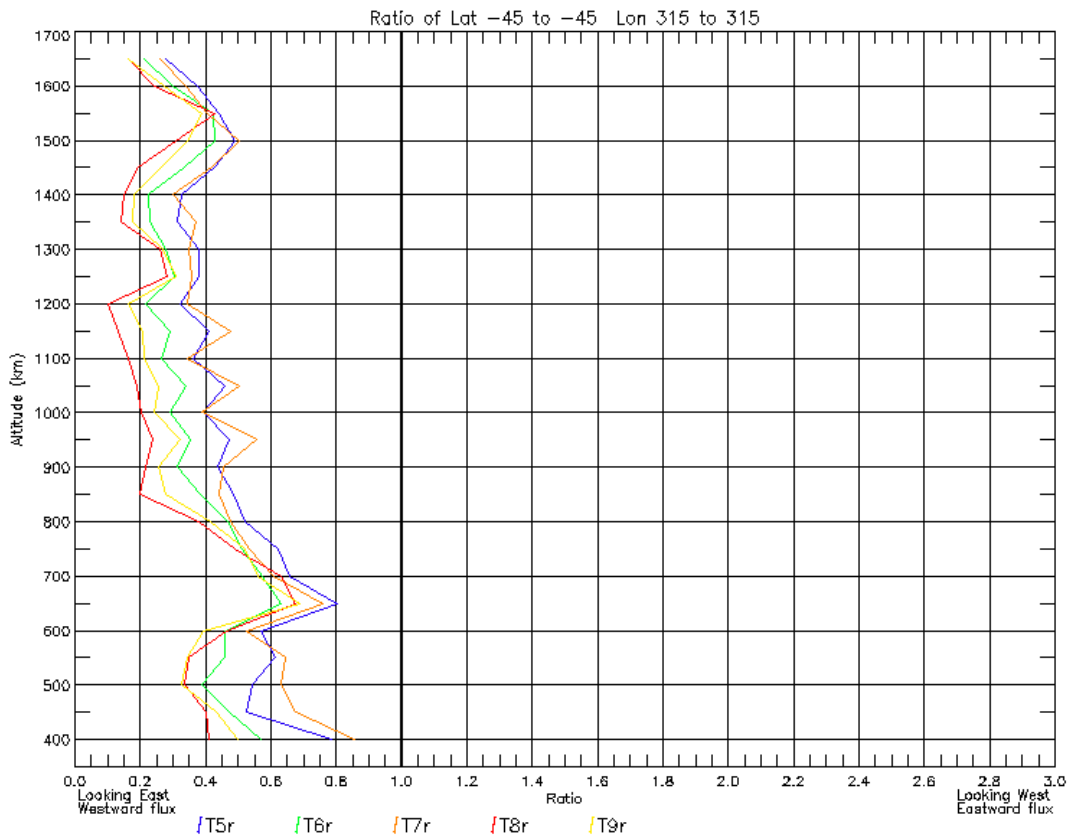
Figure 3.5: Plots of j_e/j_w ratios for energy channels T5 through T9 in the vertical stack of -45° Lat, 315° Long bins

In comparing Figures 3.2, 3.4, and 3.5 a trend begins to emerge. The ratios of measurements taken at -45° S latitude appeared to be the most offset, with ratios at -30° latitude

showing a lesser offset, while ratios at -6° latitude showed no offset at all. In other words, the

more southern measurements appear to be offset further towards a westward ratio than

measurements taken in the north. This would imply that the cause of the offset is somehow

related to latitudinal changes.

While there were many factors that changed across latitudes, one of the most drastic

changes was the average pitch angle sampled by CEASE. Figure 3.6 is a contour plot showing

CEASE's alignment with the Earth's magnetic field, in terms of its pitch angle. As stated in

Section 1.3.6, a pitch angle of 90° is desirable for optimal proton measurement. Figure 3.6 shows

that the average pitch angles at northern latitudes were between 60 and 90 degrees resulting in

close to optimal conditions. Meanwhile average pitch angles at central latitudes were between 30

and 60 degrees while the pitch angles at the southern latitudes were between 10 and 40 degrees.

This plays an important role because at any given point the majority of the proton flux has a pitch

angle of 90°, for both eastward and westward fluxes (see Figure 1.11).
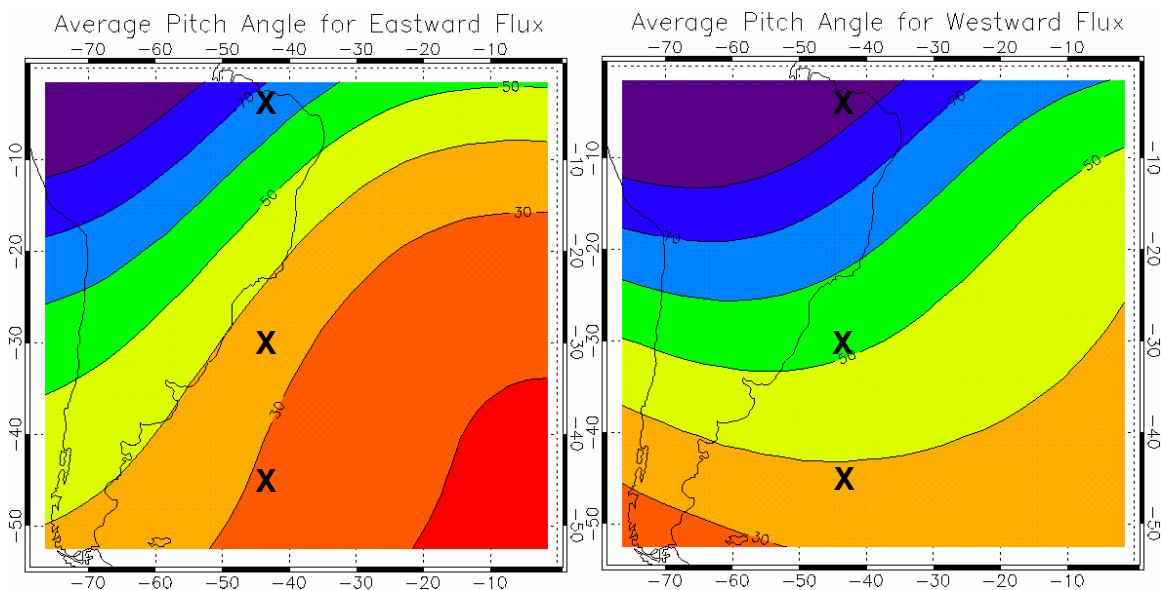
Figure 3.6: Comparison of average pitch angle for eastward flux measurements (left) and westward flux measurements (right) for a range of bins at 400 km altitude. Approximate locations of the -45°S/315°E, -30°S/315°E, and -6°S/315°E are shown as Xs

While the decrease in average pitch angle certainly corresponds to the amount of

westward offset, it does not explain why the offset is there to begin with. The offset is being

caused by the relative difference between the east-looking and west-looking average pitch angles.

Figure 3.6 shows that for most locations there is a significant difference in the look angle between

the two sets of measurements. Figure 3.7 details this difference for the -30° Lat, 315° Lon bin, by

plotting the pitch angle of the average east-looking and average west-looking pitch angles of the

CEASE instrument for every altitude. For instance, at 400 km altitude, the looking-east pitch

angle is ~36°, while the looking-west pitch angle is ~53°, resulting in approximately a 15°

difference in the average pitch angles. Furthermore, the east-looking pitch angle is closer to 90°,

which would suggest (based upon pitch angle distribution) higher westward flux measurements.

This, in turn, would result in Figure 3.2 showing a bias towards lower east-west ratios, potentially

explaining the offset.

Average Pitch Angle
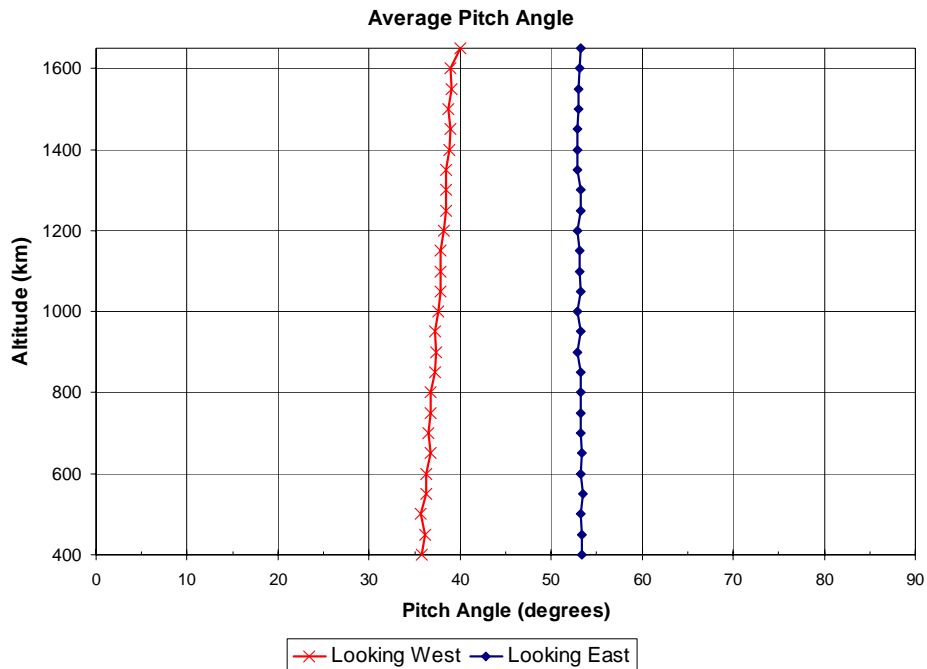
Figure 3.7: Average pitch angles of the CEASE primary look vector for east and west looking measurements in the -30° Lat, 315° Long stack at each altitude

A further examination of Figure 3.7, reveals that the angle between CEASE's primary

look vector and the magnetic field only slightly as altitude increases. At all altitudes, however, there remains a significant difference between the pitch angle sampled when looking east versus looking west. This explains why all altitudes experience some degree of offset.

Figure 3.8 shows the average pitch angles corresponding to the stack at -45° Lat, 315° Long, which corresponds to Figure 3.5 shown earlier. This bin had one of the lowest average satellite pitch angles in the South Atlantic Anomaly. Specifically, Figure 3.8 shows that the eastward flux was measured while CEASE was pointing at a pitch angle of just ~29°. Because of the low proton population expected at that pitch angle, there is now a potential explanation as to why Figure 3.5 had such low east-west ratios at nearly all altitudes for this stack of data.
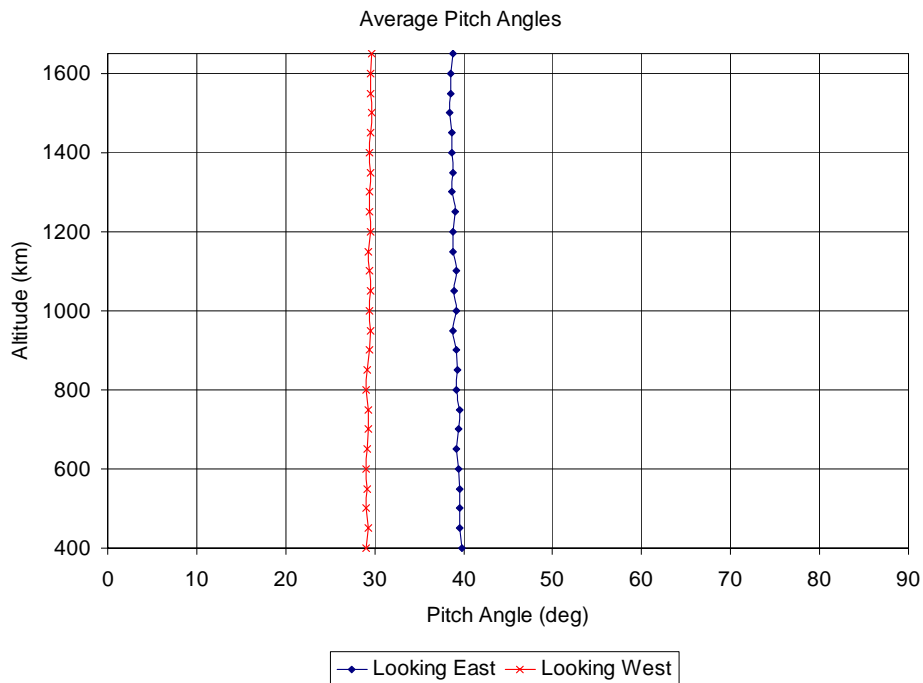
Figure 3.8: Average pitch angles of the CEASE primary look vector for east and west looking measurements in the -45° Lat, 315° Long stack at each altitude

Contrast this to Figure 3.9 which shows the different pitch angles for a stack of bins near corresponding to -6° Lat, 315° Long, where the pitch angles for both the eastward and westward flux are extremely high. As seen in Figure 3.4, in this region, the eastward flux dominates at all

altitudes, providing the clearest example of the East-West Effect, apparently free from the effects of the pitch angle related mechanism at work. Since the fall-off of the pitch angle distribution curve is less severe closer to 90° (Figure 1.11), the difference in particle populations would be lessened. Given a sufficiently large field-of-view, it's possible that CEASE could measure the peak proton population, even at the east-looking pitch angles.
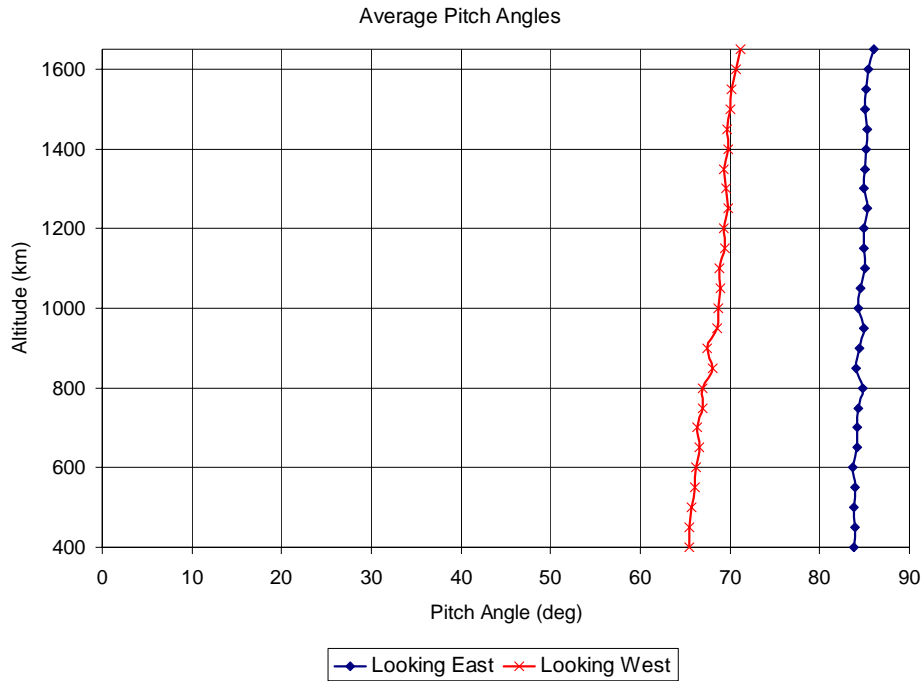
Figure 3.9: Average pitch angles of the CEASE primary look vector for east and west looking measurements in the -6° Lat, 315° Long stack at each altitude

Based upon the contrast between Figures 3.8 and 3.9, we conclude that the observed anisotropy was partly due to inconsistencies in pitch angle sampling. Furthermore, the satellite pitch angles were found to vary latitudinally, meaning that the extent of offset caused by the pitch angle difference effect also varies latitudinally.

Section 1.3.6 explained how this pitch angle difference effect is partly caused by the distribution of protons at various pitch angles. Unfortunately, that simple analysis fails to take into account the actual view factors of the CEASE telescope. The telescope is generally

considered to have a 90$^\text{o}$ field-of-view. Thus, a telescope pointed at 29$^\text{o}$, would still be able to detect particles at pitch angle over 70$^\text{o}$. In fact, for most measurements the telescope is able to detect the peak 90-degree populations while looking both east and west.   So long as the instrument can detect protons from that population, those counts would easily dominate the measurement, negating the effect of the detector not looking exactly at 90$^\text{o}$.

This led to the theory, advanced by Dr. Bronek Dichter, that something must be affecting the telescope's ability to detect particles in the 90$^\text{o}$ pitch angle population. Currently, it is believed that when CEASE's primary look vector is not at a pitch angle of 90$^\text{o}$, the proton fluxes will strike the detector at a diminished angle of incidence, affecting the count rates.

Consider the low-energy channel, T5. As discussed in Section 1.3.3, the CEASE telescope is comprised of two solid state detectors in a shielded case. Channels T5, T6, T8, and T9 all require that a proton strike both the front and rear plate in order to be detected. When the CEASE instrument is looking close to a pitch angle of 90$^\text{o}$, the most likely path for protons to follow is through the W collimator. Since T5 is a low-energy channel, the high-energy protons will not deposit enough energy in the detectors to be recorded resulting in a count of low energy protons. At angles further from 90$^\text{o}$, however, the more likely route for protons to strike the detectors require that they travel through the shielded case. Since only the high-energy protons are capable of this, T5 begins counting higher energy protons.

For channels designed to record high-energy protons, such as T8 and T9, a similar problem occurs in that as the angle of incidence to the detector increases, the energy required to travel through the wall of the detector increases. This led to the conclusion that CEASE becomes less capable of detecting low-energy protons as the angle of incidence with the protons increases. Since most of the protons are traveling at a pitch angle of 90$^\text{o}$, the angle of incidence will increase as the sampled pitch angle deviates from 90$^\text{o}$. Thus, based upon the difference of pitch angles

45

between looking east and looking west seen in Figures 3.7, 3.8, and 3.9, it appears that CEASE is more capable of detecting lower energy protons while looking east than looking west. Since there are far more protons with lower energies than higher energies, this would lead to an energy and pitch angle dependent instrument response.

Assuming that the only dominant effects at work in the data are the energy-dependent incidence angle effect (shown above) and the East-West Effect (which will be shown in Section 3.3), then it should be possible to calculate the impact of the pitch angle difference upon the measurements. As noted above, the offset in Figures 3.2, 3.4, and 3.5 can be characterized by the relative difference in the pitch angles of the satellite while looking east or west. Figures 3.7, 3.8, and 3.9 show that the pitch angles are roughly uniform in altitude, meaning that the angle of incidence is roughly uniform at all altitudes. Since the East-West Effect should taper out at higher altitudes, whatever ratio exists at the higher altitudes must be that of the energy-dependent pitch angle difference effect.

This theory is supported by Figures 3.2 and 3.4 which show an approximately steady-state j_e/j_w ratio above ~700 km altitude. This would imply that the East-West Effect is primarily confined to altitudes less than 700 km, while the pitch angle difference effect is the sole factor offsetting the ratio from 1.0 above 700 km. That being the case, it might be possible to develop a modeling tool that will correct the offset in the east-west ratios, making use of the relationship between angle of incidence and the east-looking and west-looking pitch angles. In fact, such a tool is currently under development by AFRL/VSBX, having been initiated as a result of this research.

3.3. The East-West Effect as Another Source of Anisotropy

While the pitch angle difference effect can account for westward offsets in the data set, it cannot explain why east-west ratios at lower altitudes are generally higher than ratios at higher

altitudes. This implies that another phenomenon is occurring, possible the East-West Effect.

Figures 3.2, 3.4, and 3.5 all demonstrate larger east-west ratios at lower altitudes than at higher altitudes. This is a result generally predicted by the East-West Effect. Strong eastward fluxes that gradual decay as altitude increases matches descriptions of East-West Effect behavior. The eastward flux's dominance could easily be the result of a fall-off in westward flux caused by atmospheric collisions. As altitude increases, the atmosphere thins out, resulting in a restored balance between eastward and westward fluxes. This is expressed in the figure by the decay of the ratios from a strong eastward flux towards more westward values of the ratio.

Figure 3.4 (-6° Lat, 315° Long) shows this behavior the best of the three figures. The channels all demonstrate a strong eastward flux at low altitudes, with the exception of 400 km. (The sharp decrease at 400 km is a feature found throughout all the data and appears to be statistical in nature, although this has not been confirmed) Furthermore, the five data channels demonstrate a similar and consistent decrease in the east-west ratio up to an altitude of ~1150 km, after which the ratio remains relatively stable at ~1.15. This decrease very much agrees with established East-West Effect theory.

Figure 3.5 (-45° Lat, 315° Long) was found to be highly affected by the pitch angle difference effect described in Section 3.2. A strong westward flux is displayed at all altitudes in the figure. Even so, the east-west ratio is larger at lower altitudes than higher altitudes. For all energy channels, this eastward flux was observed to diminish as altitude increases, leading to some constant value above ~1200 km, in accordance with the East-West Effect.

Consequently, it appears as if all three figures indicate the general presence of the East-West Effect. However, a qualitative similarity does not confirm the presence of the effect. To that end, a theoretical model was used to compare TSX-5 data to calculations of the predicted values based upon the East-West Effect. This would provide a quantitative determination as to whether the anisotropy detected at lower altitudes was being caused by the East-West Effect.

47

To accomplish this result, the theoretical model was constructed as referenced in Section 2.1.5. To better recreate the TSX-5 data, atmospheric and magnetic models of the locations and times of the measured data were used for consistency. Solar flux and magnetic field values corresponding to the measurements in question were used in the theoretical calculations.
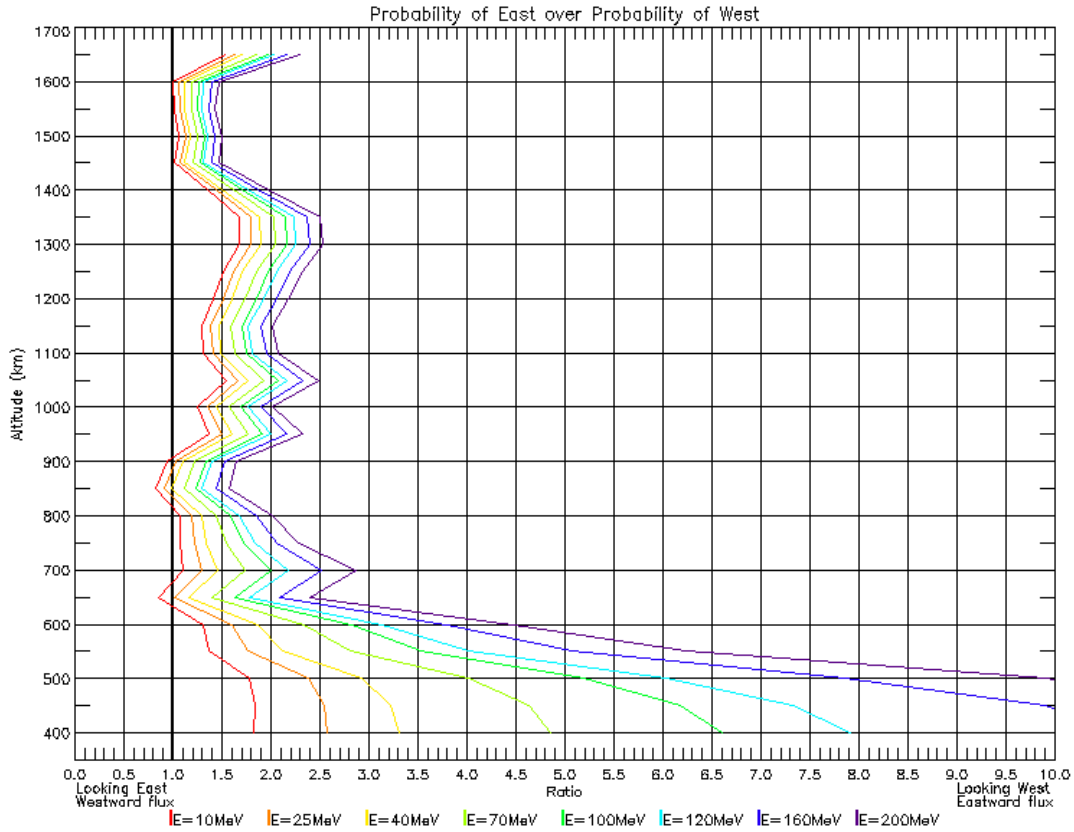
Figure 3.10: Plot of theoretically calculated east-west ratios for vertical stack of -30° Lat, 315° Long bins for 8 discrete energy levels

Figure 3.10 shows the result of the theoretical model for the stack of bins from -30° Lat, 315° Long. First, it is noted that the 160 and 200 MeV energy channels exceed the range of the plot, even though the ratio was extended all the way to 10. However, only two channels can even detect protons with energies that high, and the number of protons at those levels is expected to be exceedingly low such that their effects are typically averaged out by the large number of protons at lower energies.

Another observation is that Figure 3.10 shows some behavior on its horizontal axis, inconsistent to the expected East-West Effect behavior. From 900 km to 1450 km altitude, a rise in the east-west ratio is observed while theory predicts values close to 1.0. This behavior was repeated throughout bins across the SAA, with minor variations in the extent and altitude range of the increase. Attempts to explain what is causing this bulge have been unsuccessful so far.

Even so, the high-altitude bulge should not affect the quantitative comparisons to the theoretical model, since the East-West Effect has only minimal impacts at that altitude. To account for this, comparisons of the theoretical graphs will only be considered at altitudes where the East-West Effect is dominant.

For instance, Figure 3.11 compares the east-west ratios of the T6 observational data with the predicted east-west ratios corresponding to 25 MeV and 120 MeV (T6's energy range per Table 1.1) for the bins at -30° Lat, 315° Long. There is a considerable discrepancy between the T6 value and its bounding limits at all altitudes. This would initially indicate that the measured data is inconsistent with the East-West Effect.

In actuality, an unaccounted factor is affecting the comparison. The failure of the observational data to fall within its predicted boundaries is because the theoretical model does not take into account the pitch angle difference affecting the data. At the time of this writing, AFRL/VSBX was working on a potential pitch angle correction algorithm that could resolve this problem. Regrettably, this algorithm was not completed in time for inclusion in this research. In the interim, another method for correcting for pitch angles is possible. It was observed in Section 3.2 that the pitch angle difference effect has the least impact at measurements taken at the northernmost latitudes of the South Atlantic Anomaly. Confining comparisons to bins from these latitudes should make it possible to compare observational and theoretical data, allowing only for a small pitch angle discrepancy.
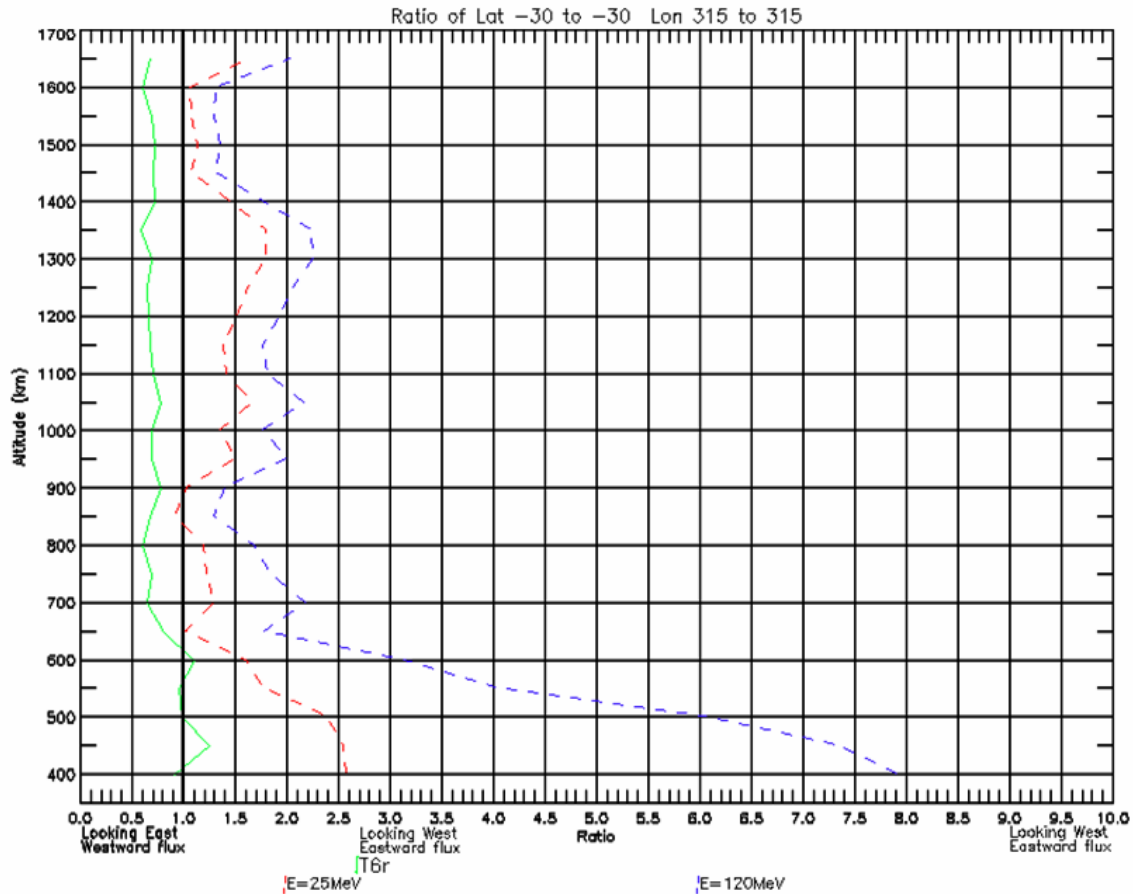
Figure 3.11: Plot of the T6 data channel (green) and the theoretically calculated east-west ratios for T6's minimum (red) and maximum (blue) detectable energies corresponding to the vertical stack of -30° Lat, 315° Long bins

To that end, Figure 3.12 shows both the measured T6 data and its corresponding theoretical limits for the stack of bins at -6° Lat, 315° Long. Here, the T6 value is shown bounded by its theoretical limits at most altitudes up to 1000 km. Excursions from the theoretical boundaries are observed at 400 km, 750km, 800km, and 850 km, however the last three are relatively minor while the first one may be the result of the unexplained westward offset at 400km that exists throughout the data set. In regards to the upper altitude excursions, its possible that pitch angle difference effects may still be having an impact, potentially causing the excursions.

50
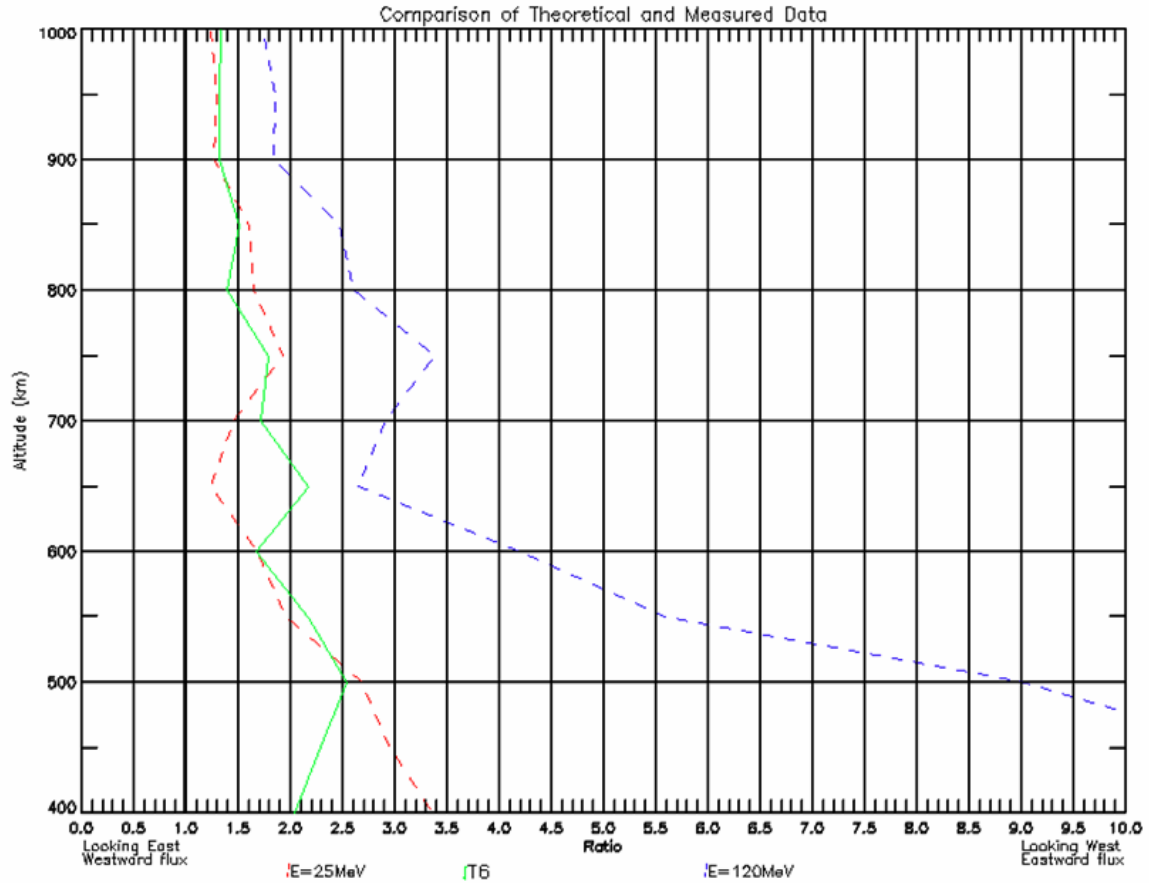
Figure 3.12: Plot of the T6 data channel (green) and the theoretically calculated east-west ratios for T6's minimum (red) and maximum (blue) detectable energies corresponding to the vertical stack of -6° Lat, 315° Long bins

Based upon the general trend for the measured T6 data to fall within its theoretical boundaries, Figure 3.12 supports the theory that these east-west ratios are a result of the East-West Effect. The fact that the T6 curve follows the lower energy limit closely further supports this claim. While the T6 data channel represents counts of protons from 25-120 MeV, there are considerably more protons at lower energies that contribute to that count. The T6 averages shown in Figure 3.12 represent this fact, and would thus be expected to trend closer to T6's lower limit, as shown.

A similar analysis was conducted for the T5 energy channel and its bounding limits (10 MeV and 100 MeV). Like the T6 average, the T5 average ratio was just slightly more eastward

than its lower limits for all altitudes up to ~1000 km altitude. All the same logic and reasoning applied to T6 would apply equally in this case. Based upon this fact, it appears that at low altitudes, both the T5 and T6 channels are accurately reflecting anisotropy within the bounds predicted by the East-West Effect.
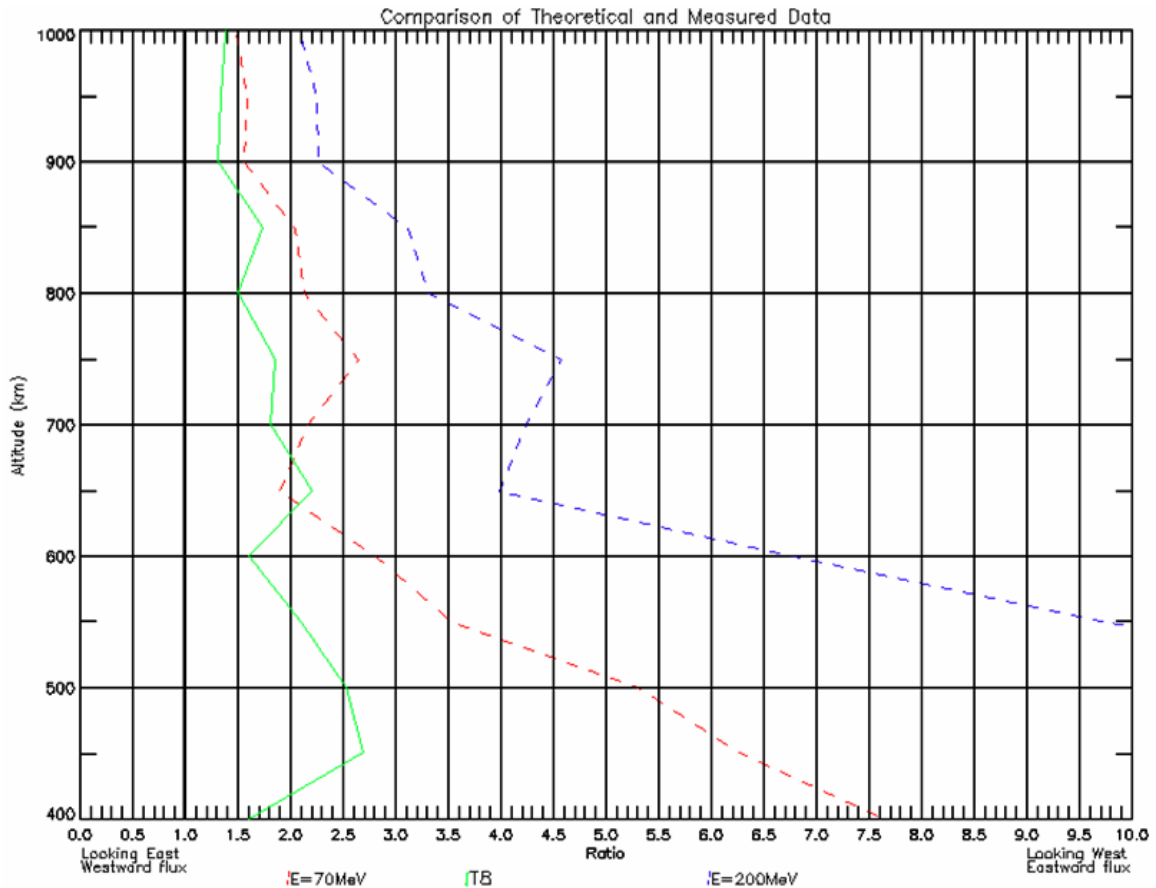
Figure 3.13: Plot of the T8 data channel (green) and the theoretically calculated east-west ratios for T8's minimum (red) and maximum (blue) detectable energies corresponding to the vertical stack of -6⁰ Lat, 315⁰ Long bins

It is only when the higher energy channels, T7, T8, and T9, are considered that the East-West Effect correlation begins to break down. First, consider T8 and T9 which demonstrate behavior similar to each other. Figure 3.13 shows the T8 data channel plotted against its theoretical minimum and maximum values (70MeV and 200 MeV respectively, per Table 1.1) for the same equatorial stack of geodetic bins. In this case, the T8 ratio averages are considerably

more westward than its minimum theoretical boundary. By 650 km, the observed and theoretical curves are closer, but the observed data still demonstrates a marked westward offset. The T9 data (not shown) is similar except that above 650 km the offset between the minimum theoretical boundary and the observed data is considerably diminished, but still present with the observed data still offset to the west.

This indicates that at higher energies, the data is not strictly conforming to the values predicted by the East-West Effect. Furthermore, since T9 represents a lower energy range than T8, the westward offset appears to be energy dependent, growing significantly between 59 MeV and 70 MeV.

The reason for the offset is that there is an additional deficiency in the model's calculations. As stated in Sections 1.3.5 and 2.1.5, the East-West Effect equations (upon which the model is based) assumes that the proton's gyro radius takes place within a relatively uniform atmosphere. This means that the gyro radius should be significantly less than the scale height for those given conditions. A quick analysis reveals that for the higher energy channels, this assumption may not hold true for the conditions being tested. Table 3.1 shows the scale height and gyro radii for a 70MeV proton at various altitudes under an arbitrary set of conditions (F10=F10A=150, Day=180, Year=2003, UTSEC=32000, Lat=-6°, Long=-54°).

At 400 km altitude, the gyro radius (56.9 km) actually exceeds the scale height (54.5 km) for this energy level, a clear violation of the assumption necessary for the theoretical calculation. Since the scale height increases much more with altitude than the gyro-radius, at some altitude the values will fall within the assumption. To determine what that value is, consider the conditions necessary for the entire circumference of the orbit to occur within approximately the same atmosphere. That would require the scale height to be approximately twice the size of the gyro-radius. From Table 3.1, that occurs around 750 km. It should be noted that in Figure 3.13, the T8 average is tracking reasonably well to the lower limit of the energy boundaries for altitudes above

750 km, albeit with a minor westward offset.

Table 3.1: Scale Height and Gryo Radii for 70 MeV protons at various altitudes under the following conditions: F10=F10A=150, Day=180, Year=2003, UTSEC=32000, Lat=-6°, Long=315°

Altitude (km)	Scale Ht (km)	Gyro Radius (km)
400	54.5	56.9
450	57.7	58.2
500	62.1	59.5
550	69.0	60.8
600	80.6	62.2
650	98.7	63.5
700	124.8	64.9
750	149.5	66.2
800	191.0	67.6
850	221.7	69.1
900	246.7	70.5
950	266.5	71.9
1000	282.4	73.4
1050	296.2	74.9
1100	308.2	76.4
1150	321.5	77.9
1200	334.5	79.4
1250	348.1	81.0
1300	362.6	82.6
1350	378.3	84.2
1400	395.2	85.8
1450	413.5	87.4
1500	433.1	89.1
1550	454.3	90.7
1600	477.0	92.4
1650	501.2	94.1

The last channel that needs to be addressed is the T7 energy channel. T7 resembles the T8/T9 trend the closest, but with several subtle differences. Figure 3.14 shows the T7 average east-west ratio and the channel's lower and upper energy limits. Like T8 and T9, there is a sharp difference in the observed and theoretical ratios at low altitudes, before it tracks well against the lower limit at mid-range altitudes. Since T7's lower energy limit is less than T9's, one would expect T7 to track closer to the boundaries than T9 does. The opposite is observed to be true.
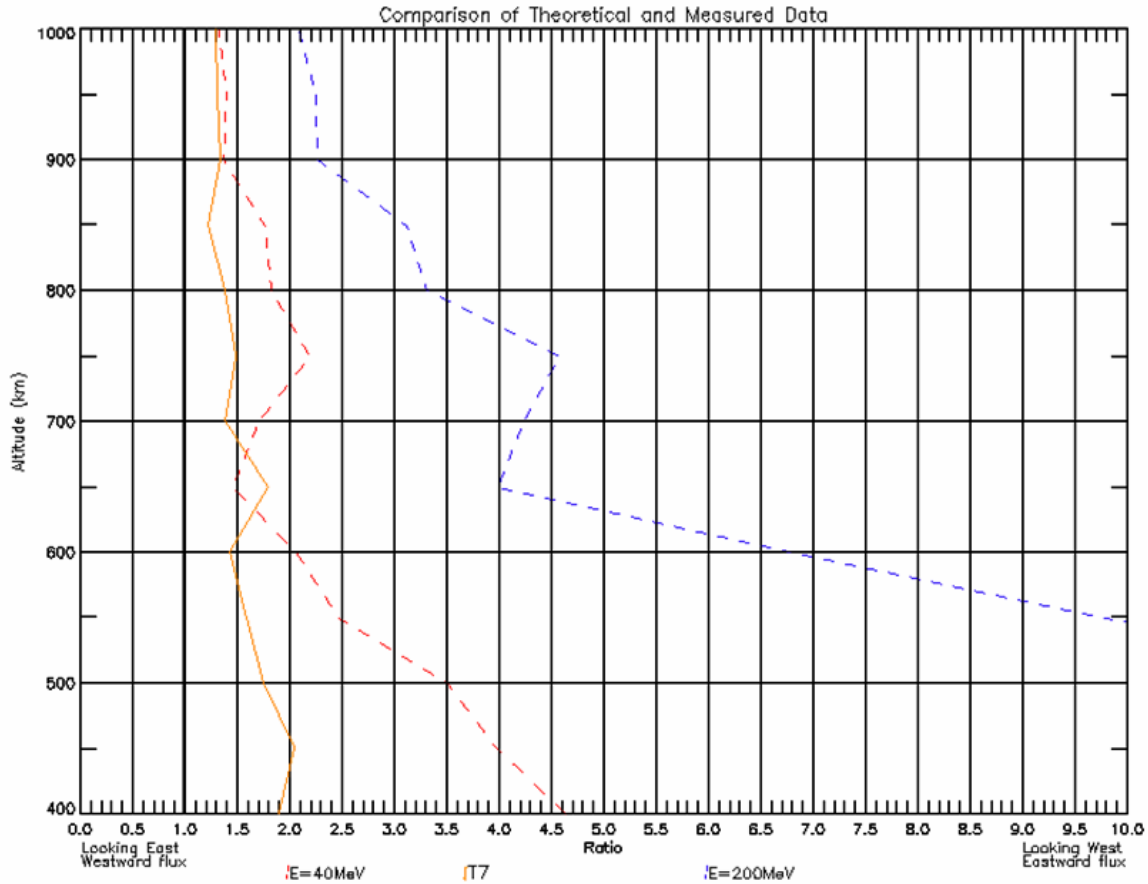
Figure 3.14: Plot of the T7 data channel (green) and the theoretically calculated east-west ratios for T7's minimum (red) and maximum (blue) detectable energies corresponding to the vertical stack of -6° Lat, 315° Long bins

This is because T7's offset is *not* being caused by the gyro radius/scale height issue causing the T8 and T9 offsets. An analysis of the scale height and gyro-radius for the T7 energy channel, under the same conditions as before, reveal that the gyro-radius (43.0 km) is well below the scale height (54.5 km). While there may be some discrepancy in the model's values, it is unlikely that this is the cause of the offset seen in Figure 3.14.

Instead, it appears that the answer comes back to the pitch angle difference effect. For low angles of incidence there is an important (but minor) increase in the effective area of the rear detector for the T7 data channel *(Dichter, private communications, 2006)*. This would allow more lower energy protons to be collected while the instrument is looking at the westward flux

than the eastward flux, resulting in a biased count in that direction. While the impact of this would be relatively minor, it may be enough of an impact to increase the offset from the theoretical curve towards the westward direction as seen in Figure 3.14.

Thus, based upon Figures 3.12, 3.13, and 3.14, there appears to be a generally good agreement between the measurement data taken by CEASE to theoretical calculations of the east-west ratios. Where differences can be found, they can be explained by errors of the model, to include violating the assumptions used by the fundamental equations of the model, or the inability of the model to take into account pitch angle difference effects. These facts generally support the conclusion that the anisotropy being observed at low altitudes is the result of the East-West Effect.

3.4. Energy Spectrum of the South Atlantic Anomaly

One more piece of evidence supports the theory that the East-West Effect is causing anisotropy within the data. Each of the data channels, T5 through T9 represent the number of protons counted by CEASE during a 5-second period over some discrete energy range. The energy range used varies per channel and allows some analysis of how the East-West Effect and pitch angle differences affect protons of various energy levels. For cases when the East-West Effect dominates (i.e.: high latitudes), it should be possible to make sure that the ordering of energy channels (which energy channel shows the highest east-west ratio), is consistent with the ordering presented in Section 1.3.5. Specifically, Figure 1.10 reveals that more energized protons will have higher east-west ratios at any given altitude. Taking the energy ranges of the T5-T9 channels into account, one would expect the channels to appear from lowest east-west ratio to highest east-west ratio in the order shown in Table 3.2.

Table 3.2: Ordering of Energy Channels in terms of increasing East-West ratio

Channel Name	Energy range of protons
T5	10-100 MeV
T6	25-120 MeV
T7*	40-200 MeV
T9	>59 MeV
T8	70-200 MeV

*T7 has a larger field of view which impacts direct comparisons of the different channels

Figure 3.4 shows the east-west ratio for channels T5 through T9 corresponding to the -6° Lat, 315° Long bin. Attempting to determine which energy channel shows the highest east-west ratio at any given altitude is a challenge, because the curves all show significant horizontal fluctuations. These fluctuations were found to be statistical in nature, and will be discussed further in Section 3.5. Furthermore, that section demonstrates how increasing the number of measurements used to derive the east-west ratios helps smooth the fluctuations out of the curves.
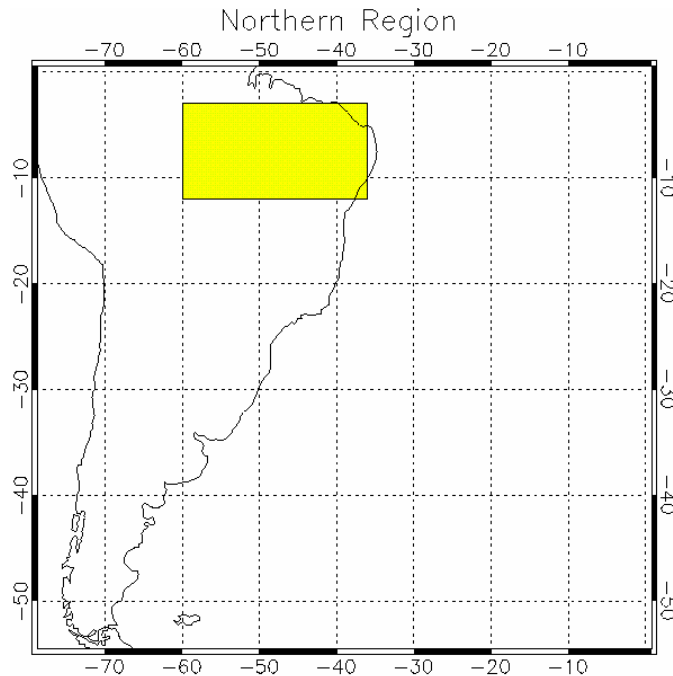
Figure 3.15: Location of the "Northern Region" including the bins from -6° to -12° Lat and 300° to 321° Long

To increase the number of measurements available for east-west ratio calculations, all the measurements from the bins -6° to -12° Lat and 300° to 321° Long were combined into a

"Northern Region," depicted by Figure 3.15. The east-west ratios at each altitude for this region were calculated by averaging the eastward and westward flux measurements across all 24 bins that comprise the region. The result was a greatly smoothed set of T5-T9 curves from which energy channel dependencies can be more easily observed.
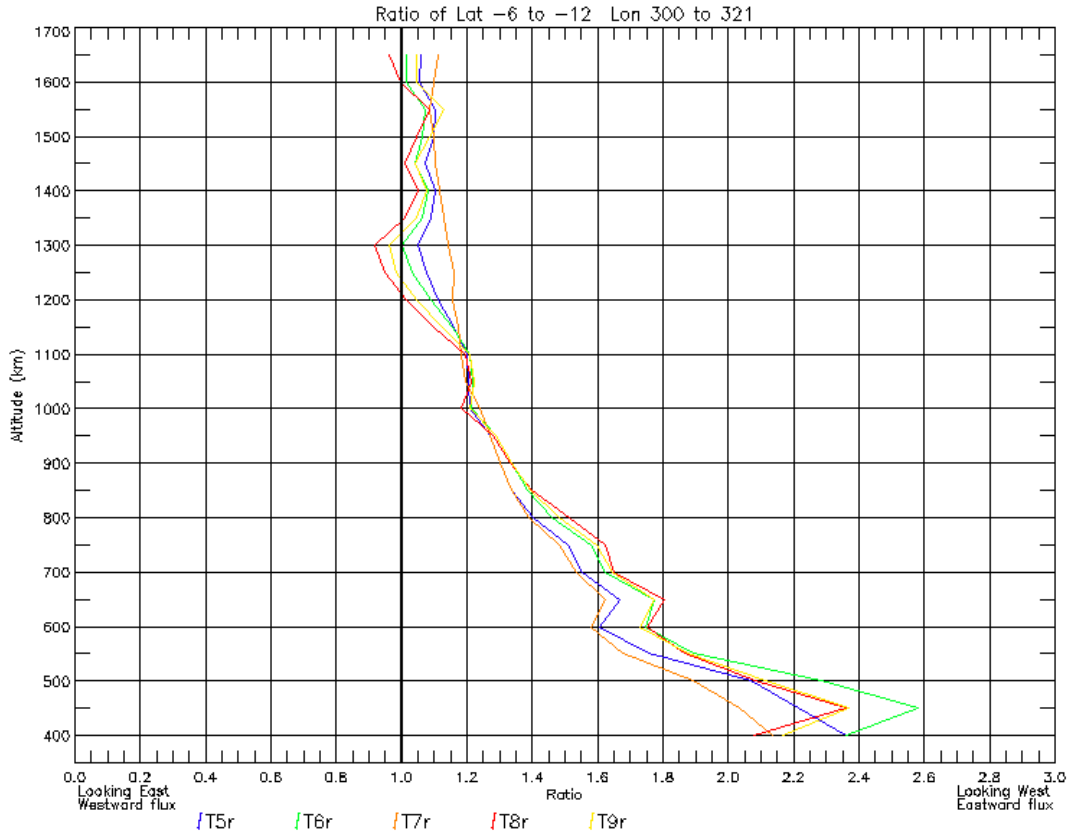
Figure 3.16: Plots of j_e/j_w ratios for energy channels T5 through T9 in the vertical stack of the northern region bins

Figure 3.16 shows the resulting east-west ratios from the Northern Region. As in Figure 3.4, the curves all start with a high east-west ratio which falls off as altitude increases, in accordance with the East-West Effect. Within this general behavior, certain trends are observed. First, although each channel shows a similar overall trend, there appear to be minor variations between them. Specifically, T5 initially shows a large east-west ratio (~2.4), but it decreases

quickly up to 600 km after which it decreases at a slower pace. At low altitudes, T7 was actually less than T5, but by 600 km, the two curves followed very similar rates of east-west ratio decrease.

In Figure 3.16, T6, T8, and T9 all have an initial spike at 450 km, but by 550 km, they all appear to demonstrate nearly identical altitude dependent behavior up to 1050 km. Below 550 km, it should be noted that T6 has the highest east-west ratio, in spite of T8 and T9 both having higher energies. This seemingly contradicts traditional assessments of how the East-West Effect operates. T8 should always have the largest east-west ratio since it has the largest gyro-radii of all the channels presented. This large gyro-radius causes the T8 protons to travel deeper into the atmosphere, increasing collisions, which should result in a higher east-west ratio. What is causing T6's ratio to exceed T8's is not understood at this time. However the sharp peak at 450 km may indicate some measure of statistical anomaly may still be occurring in spite of a large number of bins being averaged.

Above 550 km, T8 becomes the dominant channel, followed by T9, T6, and T5. This trend correctly represents that expected by Table 3.2, with the exception of T7. While T7 has a higher energy range than T5 and T6, it is capable of measuring protons from a wider field of view because protons don't have to hit the DFT for that channel. Thus, it is harder to compare T7 with the other channels, because of the additional field-of-view factor at play. These facts taken together would seem to further confirm that the anisotropy in the plots below ~1050 km altitude is being primarily caused by the East-West Effect.

Above 1050 km, the east-west ratios invert. Of the dual-detector channels (T5, T6, T8 and T9), T5 dominates while T8 actually shows a slight westward ratio. In fact, with minor exceptions, the curves above 1050 km indicate that the east-west ratio becomes stronger as average proton energy decreases. This contradicts the predicted East-West Effect behavior established in Figure 1.10 which indicated that the east-west ratios should remain roughly

constant through this region with T8 continuing to dominate. The predicted behavior is a consequence of the atmosphere having less altitudinal variation above 1050 km, resulting in similar collisional loss rates for eastward and westward fluxes at those altitudes.

Since the East-West Effect should not be dominant at these altitudes, this ordering might correspond to the impacts of the pitch angle differential, which still exists at these altitudes. However there are problems with this assumption. At near-equatorial latitudes, CEASE is looking very close to a pitch angle of 90° when looking east. This should correspond to the highest concentration of particles, meaning that CEASE is measuring westward flux under optimal conditions. The west-looking conditions measure a pitch angle near 75°, meaning that there should be a ratio favoring westward flux (j_e/j_w <1.0). This ratio would be reduced in the higher energy channels, however, since the more energetic protons have a higher likelihood of penetrating the instrument's shielding and being recorded.

Figure 3.16 shows results contrary to this expectation. While the higher energy channels do correspond to a flux ratio close to 1.0, the lower energy channels show an increasing eastward ratio, not westward (T5=1.05 at 400 km vs. T8=0.95). This trend is observed both in individual bins and in the regional analysis shown above. What is causing this inversion towards eastward flux is not understood at this time and requires further investigation.

3.5. Concerns about Statistical Sample Size

One last observation from the plots of individual bins is that there is considerable "jaggedness" in nearly all of the plots. Rather than a smooth trend towards less eastward flux, individual altitudes experience eastward or westward peaks on a seemingly random basis, as in Figures 3.2, 3.4, and 3.5. One possible explanation for these peaks is forwarded. Each data point in the plots is a ratio of the average eastward flux over the average westward flux for one bin at one altitude. The data points contributing to those bins are not evenly dispersed throughout the

timeline of the mission, but are grouped into instances when the satellites orbit took it through the given bin. On any given pass, the satellite takes either east-looking or west-looking measurements, but not both. If the satellite happens to experience anomalous conditions for one satellite pass, it's possible to bias a large number of data points, thus skewing the average.
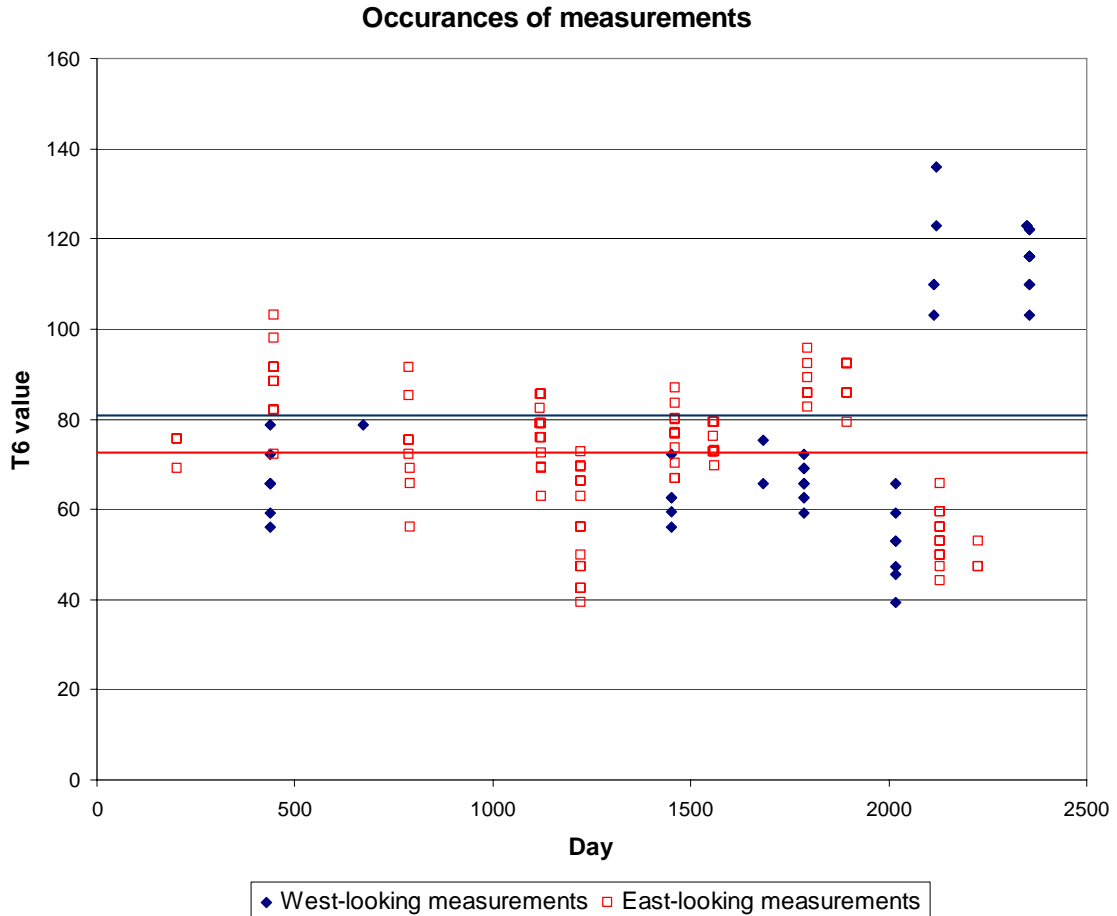
Figure 3.17: Measured T6 values and date of measurement (1 Jan 00 = Day 1) for east-looking (red) and west-looking (blue) cases in the geodetic bin at -30° Lat, 315° Long, 600 km altitude. Solid lines represent mission-span averages of the east-looking (red) and west-looking (blue) values

The result of this expanded data set is Figure 3.18. Also shown on the plot are the F10 and F10A values which serve as a proxy of solar activity over this same time scale. From the figure, the previously observed peaks are still present, but part of a considerably broader series of passes reflecting both higher and lower counts across the series of satellite passes. Further, an

inverse correlation to F10A appears such that the broadest west-looking measurements appear to

have been taken during periods of low F10A values. East-looking values appear also to have

been affected at this low F10A period, but mostly by the inclusion of lower values, not higher.

This would imply that anomalous data points in individual bins may be the result of solar cycle

variations.
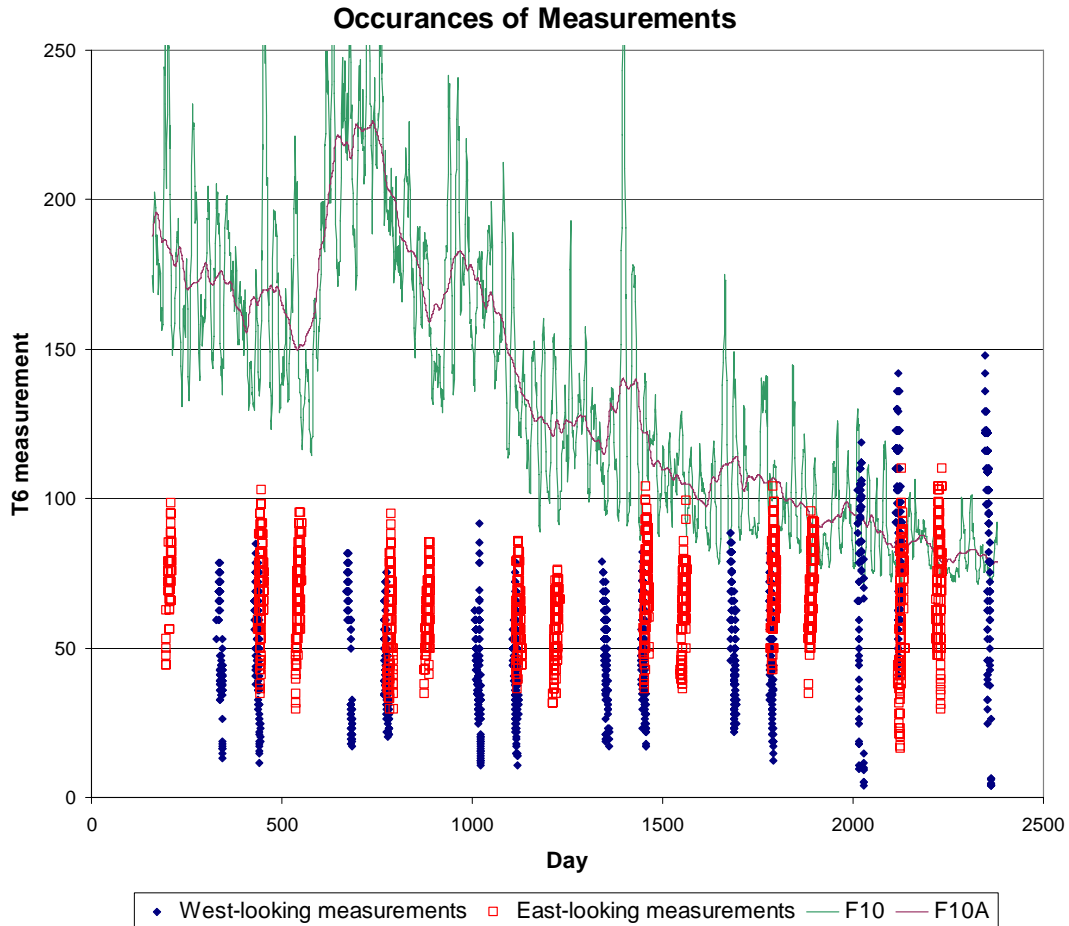
Figure 3.18: Daily F10 value, average F10 value, and measured T6 values (west-looking and east-looking) plotted by date of measurement (1 Jan 00 = Day 1) for the geodetic bins from -27° to -36° Lat and 309° to 321° Long at 600 km altitude

If the altitude analysis of east-west ratios is conducted again using all these measurements

(such as Figure 3.16), the jaggedness is considerably reduced compared to what was seen in the

individual bins, as seen in Figure 3.19. Here, the general trend towards higher eastward fluxes

can be seen in all data channels at lower altitudes, gradually diminishing to a steady-state value

by ~1000 km altitude. This basic pattern fits the accepted theory of the East-West Effect albeit

with an offset caused by the apparent pitch angle difference effect.
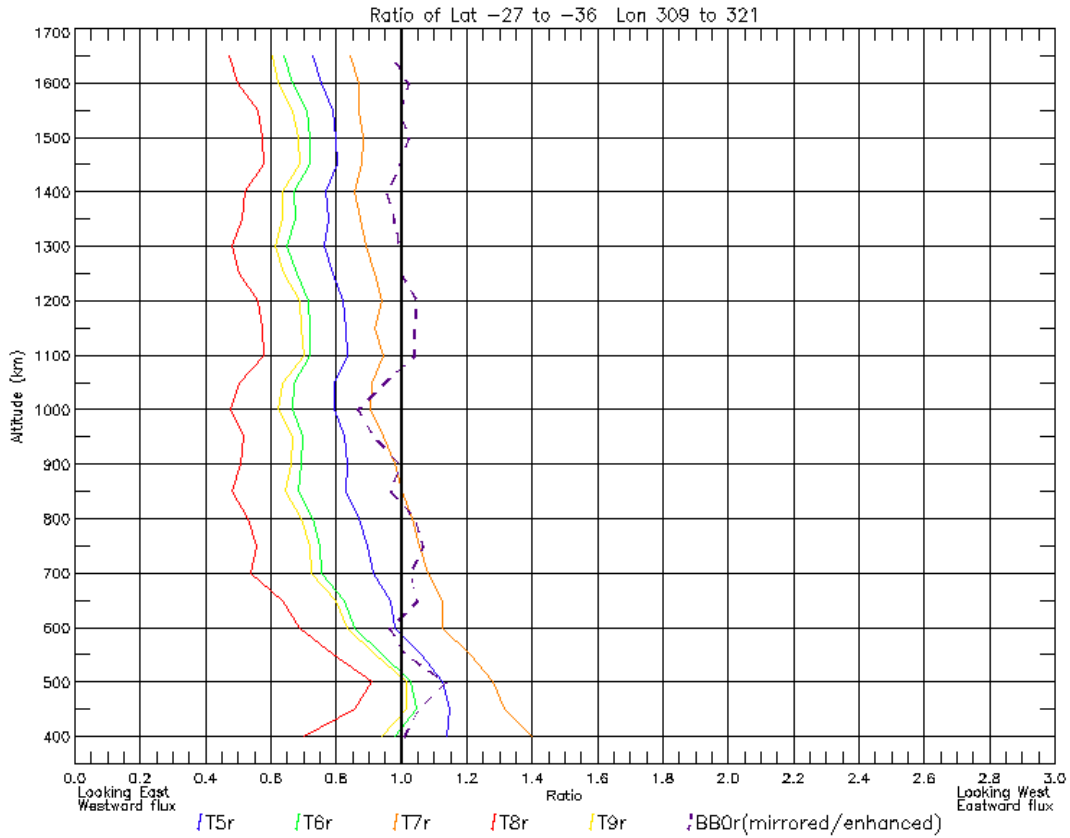
Figure 3.19: Plots of j_e/j_w ratios for energy channels T5 through T9 in the vertical stack of the central region bins

Another possible explanation for the anomalous data points in Figures 3.17 and 3.18 is

that TSX-5 started to have some spin-stabilization issues towards the end of its mission (*G. Ginet*,

private communication, 2006). While this may be an issue, there is further evidence outside of

the CEASE data set to suggest that solar cycle variability was the primary cause. Figure 3.10

depicted the east-west ratios for several energy levels based upon theoretical calculations. Such

calculations would not have taken into account spin stabilization issues experienced by TSX-5.

In Figure 3.10, jaggedness similar to that seen in Figures 3.2, 3.4 and 3.5 can be seen at various

63

altitudes. Furthermore, such jaggedness was found throughout the plots of theoretical data. Since the theoretical ratios are constructed from the F10 and F10A values corresponding to dates of CEASE measurements, it's possible that solar cycle variations could lead to anomalously high and low data points in those calculations as well.

To test this, a plot of theoretical east-west ratios was made for the Central region (-27° to -36° Lat and 309° to 321° Long), and is shown in Figure 3.20. As in the case of the observed data (Figure 3.19) this largely resolved the jaggedness issues, giving further credence that the jaggedness is a statistical phenomenon caused by some factor (such as solar cycle variability) affecting both the observed and theoretical data sets.
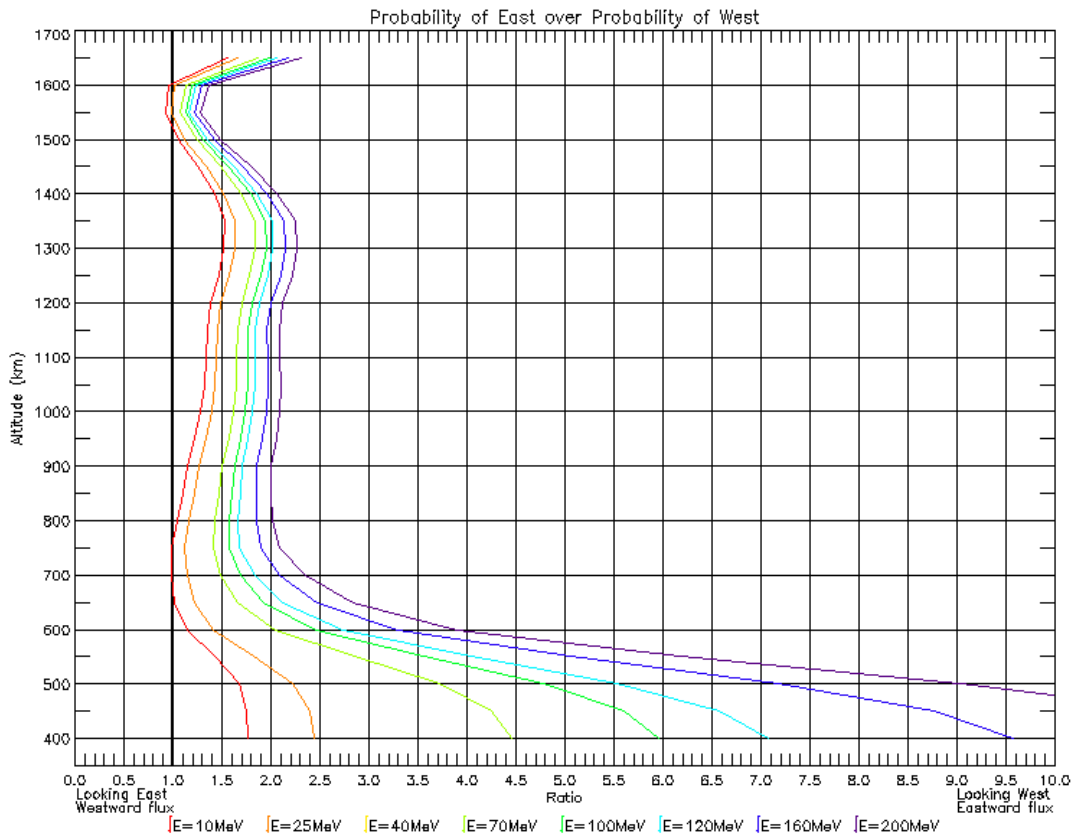
Figure 3.20: Plot of theoretically calculated east-west ratios for vertical stack of bins in Central Region for 8 discrete energy levels

Averaging across multiple bins apparently adds more measurements which smoothes the

result, but also adds a new complexity. Figure 3.21 shows the average pitch angle for the set of 20 bins that comprise the Central region. The bars around each average show how broad the spread of pitch angles is that comprise that average. With such a broad range of pitch angles used to calculate the average, it becomes exceedingly difficult to analyze the effects of pitch angle variability throughout the South Atlantic Anomaly on a regional scale. Furthermore, should a correction for the pitch angle offset be developed, it would be inadvisable to apply the correction to the regional averages, since the individual bins comprising the region would be impacted to different degrees.
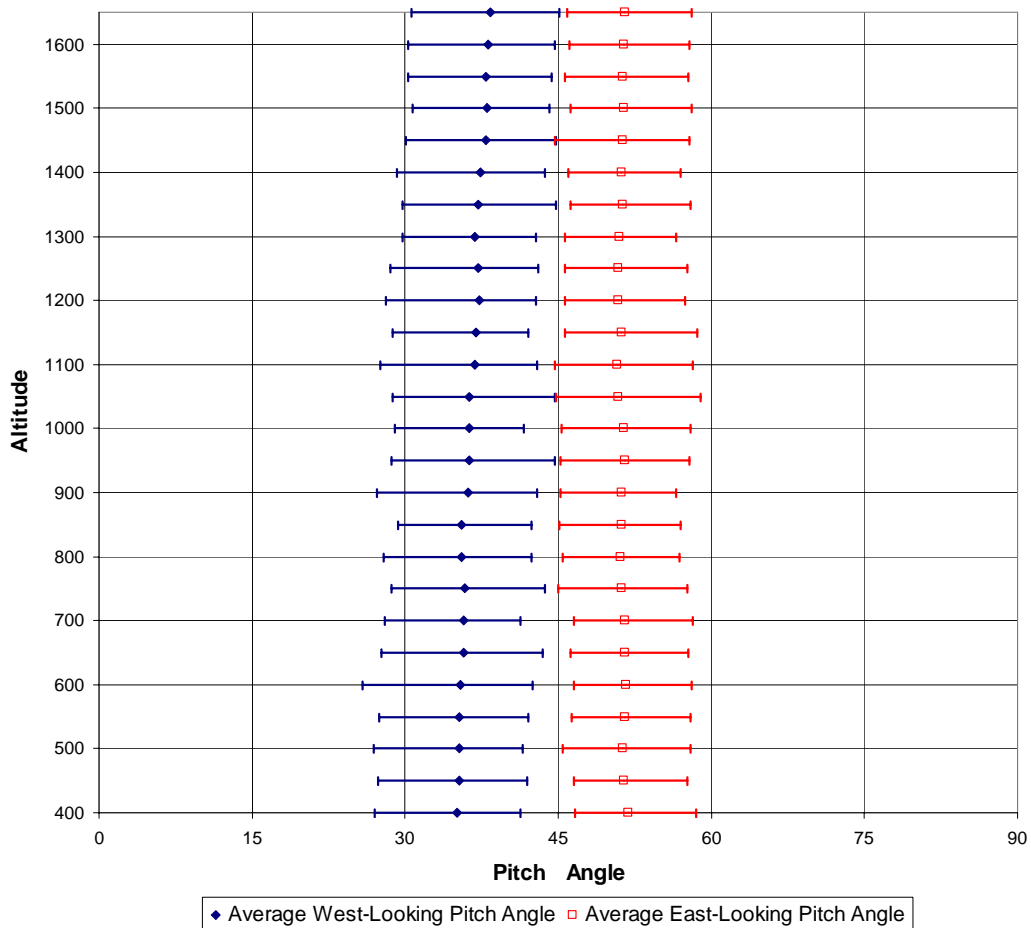
Figure 3.21: Distribution of average pitch angles for the bins comprising the Central region at each altitude for eastward flux (blue) and westward flux (red) measurements

A solution to these issues would be to develop a new binning scheme. Ideally, the data

would be resorted to increase the size of the bins, making them large enough to average out statistically high or low satellite passes while remaining small enough to allow pitch angle effects to be measured and corrected. One potential drawback to a new binning scheme would be that other factors such as magnetic field orientation, magnetic field intensity, or L shell might be made too broad, limiting future studies of the data.

Another solution would be to divide the CEASE data into solar max and solar min subsets. Such a scheme could greatly reduce the impact of solar cycle variability within the data sets. Unfortunately, unless the bins would be resized, dividing the existing data set into two subsets would result in fewer data points per bin. This could lead to new statistical errors, because of an inadequacy of data points.

Because of these and other concerns, the issue of resizing the geodetic bins remains unresolved at this time.

IV. Conclusion

4.1. Anisotropy in the South Atlantic Anomaly

A careful analysis of the TSX-5 data provided by AFRL/VSBX does reveal that there is a strong anisotropy being recorded within the South Atlantic Anomaly. Contrary to the hypothesis, however, the anisotropy was only partly the result of the East-West Effect. Section 3.3 showed that protons near the equator were being recorded in an east-west ratio consistent with the East-West Effect for most energy levels. Specifically, the average T5 and T6 ratios were shown to follow the east-west ratios predicted by the East-West Effect through a variety of altitudes. For T7, T8 and T9, the curves followed the correct trend, albeit with a westward offset. The most likely cause of this offset is the inability of the model to characterize east-west ratios at high energy levels. Section 3.4 also demonstrated that even though the high-energy channels couldn't be quantitatively verified, they did follow the correct curve shape and were ordered in the appropriate sequence predicted by the East West Effect; channels measuring higher energy showed stronger east-west ratios because the westward flux protons dipped lower into the atmosphere increasing their chance for collisions.

The second, unanticipated source of anisotropy in the South Atlantic Anomaly was identified in Section 3.2 as an observational bias caused by not measuring protons at a consistent angle of incidence. The orientation of TSX-5 caused measurements of the eastward flux and westward flux to be taken at two different pitch angles resulting in the main flow of protons striking the CEASE instrument with angles of incidence that varied ~15° between east-looking and west-looking measurements. In all cases, the westward flux measurements impacted the detector at an angle closer to 90°, allowing CEASE to count more of them. Furthermore, the angles of incidence varied with respect to latitude such that measurements taken at southern latitudes had exceedingly small angles of incidence while measurements taken near the equator

were the closest to 90°. These factors contributed to a latitudinal-dependent, energy-dependent westward flux bias in the east-west ratio present at all altitudes. Identification of this observational bias led to an on-going study at AFRL/VSBX into the energy-dependent response of CEASE to protons striking it at various angles of incidence.

One final conclusion was that the time-independent 3° x 3° x 50km technique may be an inadequate binning arrangement for future studies of the South Atlantic Anomaly. Section 3.5 showed that anomalously low or high data points may be affecting the averages used in this research, due to the limited number of measurements being used to derive these counts. This occurs because all the data points are arranged in clusters caused by satellite passes through the individual bins. While individual high or low data points might average out, a cluster of 4-10 of them from just one intense satellite pass can heavily impact averages used to analyze the data. Additionally, Figure 3.18 showed that many of the exceptionally high or low proton counts occurred during measurements taken near solar minimum. This may mean that future studies may want to consider solar maximum and minimum data separately. Doing so, would require considerably larger bins, however, to account for the decrease in data points that would result from splitting the data into smaller subsets.

4.2. Applicability Towards SAAMAPS

The ultimate goal of this research was to resolve the source of anisotropy in the TSX-5/CEASE data so that an updatable model of the South Atlantic Anomaly could be developed. To that end, this research has been partially successful. One source of anisotropy was positively identified and proper application of modeling techniques should be able to correct for the anisotropy in the dataset.

More importantly, another unanticipated source of anisotropy was also detected. Since the anisotropy is a consequence of observational bias, there is no easily applicable theory or

equation to correct for its effects. We were able to respond to requests from scientists at

AFRL/VSBX, however, and provide them with the necessary data to create an algorithm that will

hopefully correct for the anisotropy.

Should these two corrections prove successful, it should be possible to create accurate

models of expected proton levels throughout the entire South Atlantic Anomaly. Such a mapping

would serve as the basis for the proposed updatable South Atlantic Anomaly model, SAAMAPS.

4.3. Areas for Future Study

This research project led to several unanswered questions which should be investigated

further. The questions fell into several broad categories including pitch-angle correction, the

theoretical model, statistical sample size, and general questions. The questions are broken out

into those categories and shown in Table 4.1

Of all the questions presented, the most critical are those related to the pitch angle

correction scheme currently being developed. It would be highly desirable to check the

effectiveness of this correction algorithm and determine if all the sources of anisotropy in the

TSX-5 data set have been identified. Furthermore, it would be beneficial to quantitatively

compare the corrected east-west ratios to the theoretically predicted ratios and determine if the

correction is providing correlation similar to that of Figure 3.16.

 The second most important issue to be addressed would be an update to the theoretical

model. The most vital update needed is the ability to accurately predict east-west ratios for the

high energy channels by calculating an average scale height across the entire gyro radius. This

would allow the northern T7, T8, and T9 data to be verified, and would serve as a useful tool for

verifying the corrected data at lower latitudes.

Beyond these two issues, there are a multitude of other questions that could be addressed.

Most of them would only serve to provide completeness to certain aspects of this report or satisfy

certain curiosities that appeared as the data and models were analyzed. While many of these issues may prove beneficial for future study of the data, the immediate impact of these other questions currently appears minimal, at best.

Table 4.1: Questions for Future Study

Pitch-Angle Correction Algorithm	What impact would AFRL/VSBX's pitch angle correction algorithm have on the average east-west ratios?
	Would this resolve the westward offsets seen in the central and southern latitudes?
	Would the northern latitude observational data still track with the theoretical calculations?
Updating the Theoretical Model	If the theoretical calculations for the East-West Effect were made to consider variable scale heights at low altitudes (i.e.: calculating the average scale height for a large number of points across the protons' gyro radii) would the T7, T8, and T9 energy channels parallel the lower energy limit like T5 and T6 did?
	What is causing the unusual bulge in the theoretical model at higher altitudes? Is it the result of statistical sampling, an error in the model's calculations, or something else entirely?
Statistics	What is an appropriate binning arrangement to correct for isolated high and low data point clusters occurring near solar minimum while still preserving pitch angle and magnetic field fidelity within each bin?
	How would comparisons of solar maximum east-west ratios compare to solar minimum east-west ratios? Would these results match accepted theory for solar cycle dependence of the East-West Effect?
General	Why are the energy levels ordered in reverse in Figure 3.14 at high altitudes?

Appendix A: How Neutral Particle Collisions Cause the East-West Effect

The East-West Effect is a phenomenon found in the South Atlantic Anomaly, which causes the protons traveling eastward to outnumber the protons traveling westward.

Section 1.3.5 describes how protons orbit magnetic field lines as a result of the first adiabatic invariant [*Sturrock*, 1994]. The radius of this rotation, a, is dependant on the charge of the particle, q, the particle's velocity (energy), $v_\perp$, the particle's mass, m_p, and the strength of the magnetic field, B, as seen in Equation A.1. Also recall the equation to convert the protons' energy to a non-relativistic velocity, shown in Equation A.2

$$a = \frac{m_p \cdot v_\perp}{|q| \cdot B} \tag{A.1}$$

$$v = \sqrt{\frac{2E}{m_p}} \tag{A.2}$$

Because of the direction that protons travel on these gyro-radii, any eastward flux will come from an orbit higher than the observation point, while the westward flux comes from an orbit below the point of observation. Figure A.1 depicts these two gyro-radii as the upper and lower curves respectively. Please note that the gyro-radii are not directly above or below the observation point. Instead, they are normal to the magnetic field vector at the point of observation.

To understand the physics behind the East-West Effect, it is useful to consider the case of 20 MeV protons traveling across these two gyro-radii. Further, consider that all of this is happening on 1 July 2003 (the magnetic field intensity and direction as well as the atmospheric density all change with respect to time). Also, assume that the observation point is at -30° Lat, 315° Long, and 450 km altitude. Given this information, we can determine what the size of the gyro-radii should be for protons on these two paths.
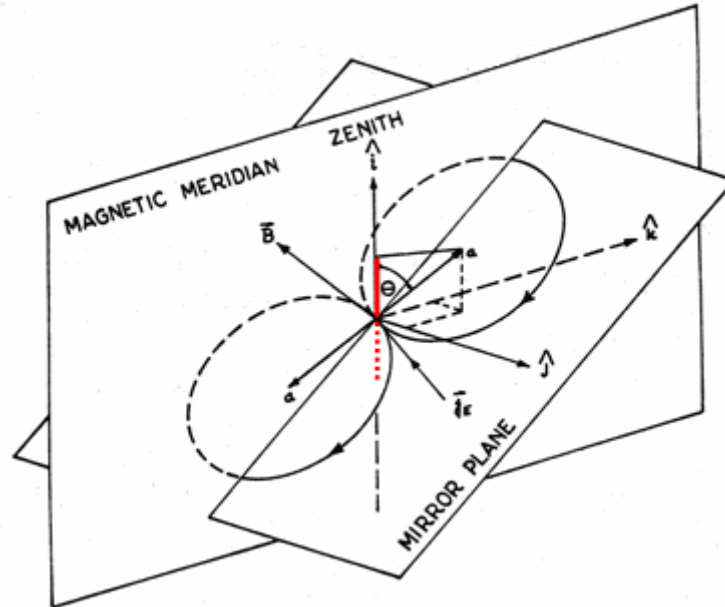
Figure A.1: Geometry showing the difference in altitude between the centers of the gyro-radii corresponding to the eastward and westward fluxes [*Heckman et al.*, 1963]

Equation A.2 yields a velocity of 6.190 x 10^7 m/s. Making use of the International Geomagnetic Reference Field (IGRF) model for the location and date assumed, the magnetic field would be 19,463 nT. Plugging the velocity and IGRF-derived magnetic field intensity into Equation A.1 produces a gyro-radius of 32.9 km. Since the proton has to travel the entire circumference of the gyro-radius, multiplying 32.9 km by 2π gives us the total distance traveled for the proton – 206.7 km.

Over the course of this path, it's possible that the proton may collide with a neutral particle. To determine the likelihood of this happening, it is useful to consider the particle's mean free path, λ_{mfp},, which describes the average distance the proton would travel before colliding with a neutral. The equation for λ_{mfp} is given in Equation A.3 [*Schunck et al.*, 1999], where v is the velocity of the proton and ν_{in} is the collision frequency between ions and neutrals.

$$\lambda_{mfp} = \frac{\upsilon}{\nu_{in}} \tag{A.3}$$

In this case, the collision frequency should be described by Maxwell Molecule collisions [*Schunck et al.*, 1999], which describe collisions between a proton (or H+ ion) and various neutral particles. Specifically, Schunck presents an updated form of the equations on page 99 that also accounts for resonant charge exchange. The problem is that the coefficients of the equation vary based upon which neutral particle is being considered. To account for this, one simplification will be used. MSIS reveals that for the altitudes in question, the dominant particle is monatomic oxygen. With a concentration of 3.079×10^7 atoms/cm^3 at 450 km altitude, O easily outnumbers the other constituents such as N_2 (7.186×10^5 molecules/cm^3) and O_2 (1.457×10^4 molecules/cm^3). Thus, for the purposes of this example, only collisions with monatomic oxygen will be considered.

Given this simplification, the ion-oxygen resonant collision frequency can be expressed by Equation A.4, where T_i is the temperature at that altitude, and n_O is the number density of monatomic oxygen.

$$\nu_{in} = 6.61 \times 10^{-11} \cdot n_O \sqrt{T_i} \left(1 - 0.047 \cdot \text{Log}_{10} T_i \right)^2 \tag{A.4}$$

Because the atmosphere is rapidly decreasing with altitude at these heights, it will be necessary to consider separate oxygen densities for the eastward and westward fluxes. Again, MSIS can be used to derive the concentrations of O needed. However, since the concentrations vary with altitude, the issue of which altitude to use in MSIS becomes a concern.

A rigorous method of determining collision frequencies might be to calculate it for every altitude experienced over the gyro-radius and take a weighted average of the result. This can be computationally intensive, particularly if a large number of gyro-radii need to be considered, as is the case in this research. Instead, *Lencheck and Singer* [1962] proposed using the atmospheric

density at the center of the orbit as an average value. This assumption works so long as the gyro-radius is considerably less than the scale height, which describes the distance needed for the atmosphere to reduce its density to 37% from the initial value. Making this assumption means that the atmospheric density is approximately uniform over the course of one gyro-radius.

The next task is to determine the altitude that corresponds to the center of the gyro-radii for both the eastward and westward fluxes. Figure A.1 shows that these values would correspond to the values shown in Equation A.5, where z_0 represents the altitude of the satellite, and I is the dip angle, which corresponds to θ shown in the figure.

$$z(\tfrac{E}{W}) = z_0 \pm a \cdot \cos(I) \qquad (A.5)$$

From IGRF, the dip angle was found to be -40.08 degrees. Using a z_0 of 450 km and a gyro-radius of 32.9km, the altitudes at the center of the eastward flux and westward flux gyro-radii are 475.2 km and 424.8 km respectively.

Using MSIS for these altitudes, this would correspond to the monatomic oxygen concentrations and temperatures shown in Table A.1. Using these values in Equation A.4, a collision frequency of 8.310×10^{-2} collisions per second is found for the westward flux and a collision frequency of 3.825×10^{-2} collisions per second is found for the eastward flux.

Table A.1: Monatomic oxygen concentrations, temperatures, and collision frequencies for the two altitudes corresponding to an eastward and westward flux gyro-radius meeting at 450 km altitude

Gyro-radius corresponding to	Altitude (km)	Number density of O (atoms/cm^3)	Temperature (K)	ν_{in} (collisions/sec)
Westward flux	424.8	4.824×10^7	918	8.310×10^{-2}
Eastward flux	475.2	1.972×10^7	918	3.825×10^{-2}

Using these values in Equation A.3, the mean free paths for the protons on the two gyro-radii are found to be 7.459×10^5 km for the westward flux and 1.618×10^6 km for the eastward

flux. This is significantly greater than the 206.7 km circular path that the protons follow, meaning that a significant number of protons will not impact neutral particles.

The mean free path is simply an indicator of the average of many possible collision lengths. In reality, collisions may and do occur and within the 206.7 km path on a regular basis, because of the number of protons undergoing these gyro-motions. In this regard, the mean free path helps identify the likelihood that a collision will happen on one of the two paths. Specifically, the longer mean free path of the eastward flux indicates that particles are less likely to have a collision than particles traveling on the westward flux with a shorter mean free path.

If we take the ratio of the two paths (eastward flux's mean free path over westward flux's mean free path), the ratio comes out to be 2.172.

Contrast this to Equation A.6 [*Lenchek et al.,* 1962] which approximates the ratio of eastward flux over westward flux for a given scale height, dip angle, and gyro-radius. Using the values derived above, the east-west ratio works out to be 2.240. This number closely matches the ratio derived above of 2.172.

$$j_e/j_w = \exp\left[\frac{2a \cdot \cos[I]}{h}\right] \qquad (A.6)$$

Based upon this comparison, the technique suggested by *Lenchek and Singer* [1962] appears to accurately account for collisional differences occurring between the protons following both the eastward and westward gyro-radii.

Appendix B: Satellite-Centered Geomagnetic Coordinate System and Clock Angles

The Earth's magnetic field is often approximated by a tilted dipole, with its north pole near the geographic North Pole. That being the case, the Earth's magnetic field will have a generally northward orientation, except at near polar latitudes, when it can have a strong vertical component as well as a southern component. In general, the South Atlantic Anomaly region considered in this research does not extend much below 48° South latitude at 400 km altitude, meaning that the Earth's magnetic field will generally point northward over our area of interest.

This simplification makes it possible to determine what direction the CEASE instrument is looking at any given point in the data set.
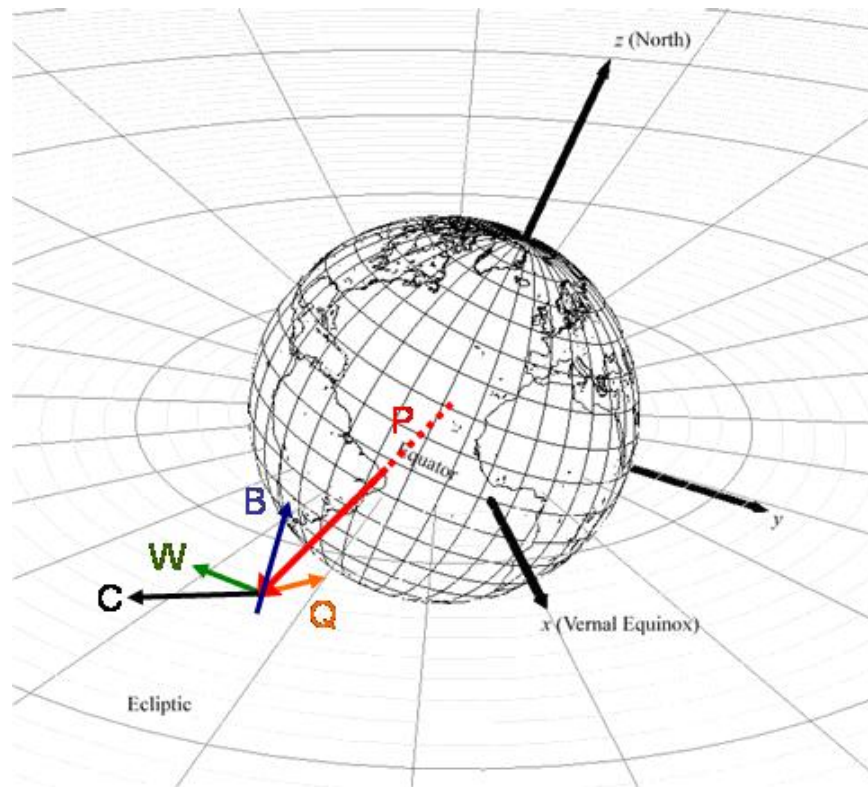

Figure B. 1: Depiction of coordinate system and vectors used to determine clock angle

Consider Figure B. 1, which gives an example of the vectors necessary for this determination. In the figure, $\bar{P}$ represents the position of the satellite, $\bar{B}$ is the magnetic field

vector at the satellite, and $\bar{C}$ is the look direction of the CEASE instrument, all in the Earth

Centered Inertial (ECI) coordinate system. These three vectors were provided by AFRL/VSBX

in the CEASE data set. From them, a vector $\bar{P} \times \bar{B} = \bar{W}$, where $\bar{W}$ is a vector that will always

point toward the magnetic west.

The orthogonal vector $\bar{Q}$ is defined by $\bar{W} \times \bar{B} = \bar{Q}$. This results in an orthogonal basis

with the WQ plane perpendicular to the magnetic field vector $\bar{B}$. In this plane, we can define a

clock angle. Taking $\bar{Q}$ as the reference point and proceeding initially towards $\bar{W}$ (a counter-

clockwise direction as seen from magnetic north), we define an angle θ, that can be used to

specify east or west relative to the magnetic field. As seen in Figure B.2, any angle between 0

and π points westward, while any angle between π and 2π points eastward. If the projection of

the CEASE look vector, $\bar{C}$, is plotted using this technique it becomes possible to identify whether

the instrument is looking east or west.
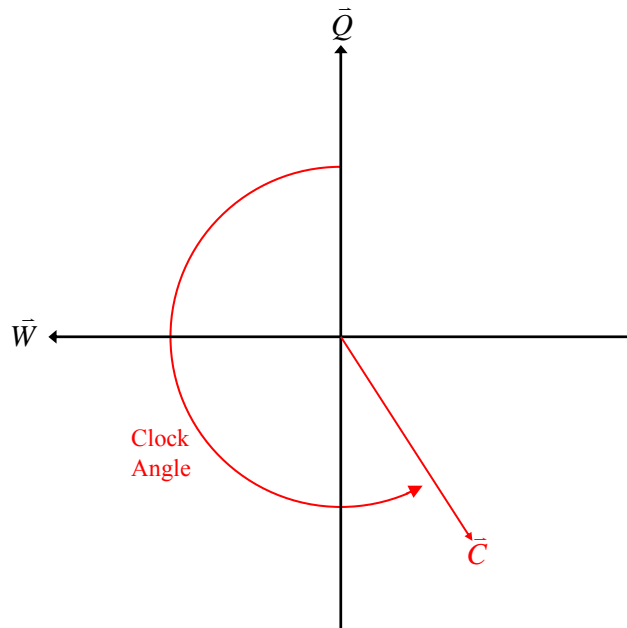
Figure B.2: Depiction of clock angle for vector $\bar{C}$ in *WQ* plane

Appendix C: Poisson Distribution Error Analysis and Error Propagation

The data collected by the CEASE instrument is heavily dependent upon probabilities and statistics. Even though TSX-5 may be in a region of high proton flux, it is entirely possible that all the protons will miss the detector, resulting in a zero count. Likewise, it also possible for TSX-5 to be in a region of low proton flux, but detect a high proton count rate if all the protons just happen to strike the detector. While such extremes are expected to be rare, they are still statistically possible, resulting in possible skews to the data set. The solution to this problem is to include a wide range of data in any average. Since the extreme cases are considerably less likely than the detector measuring the actual flux, an appropriately large sample size should yield average measured values close to actual average.

Even with a large sample size, it is likely that the measured average will not equal the actual average. To account for this it is necessary to include error bars around the measured average such that the actual average will likely fall within the range of acceptable error. To decide what technique should be used to determine those error bars it is first necessary to decide what sort of distribution is being represented by the data.

Consider Figure C.1 which shows all the non-proton event instances of east-looking and west-looking measurements for the -30° Lat, 315° Long, 1000 km bin and the day which they occurred. Blue and red lines are also shown in the figure representing the average count/5-sec values for east- and west-looking measurements, respectively. The plot shows that most of the data points lie near their respective average, with some "outliers" considerably farther away. It is important to realize that the deviations between the data points and the average may be a result of either measurement variations (as mentioned above) or random fluctuations in the actual number of protons.
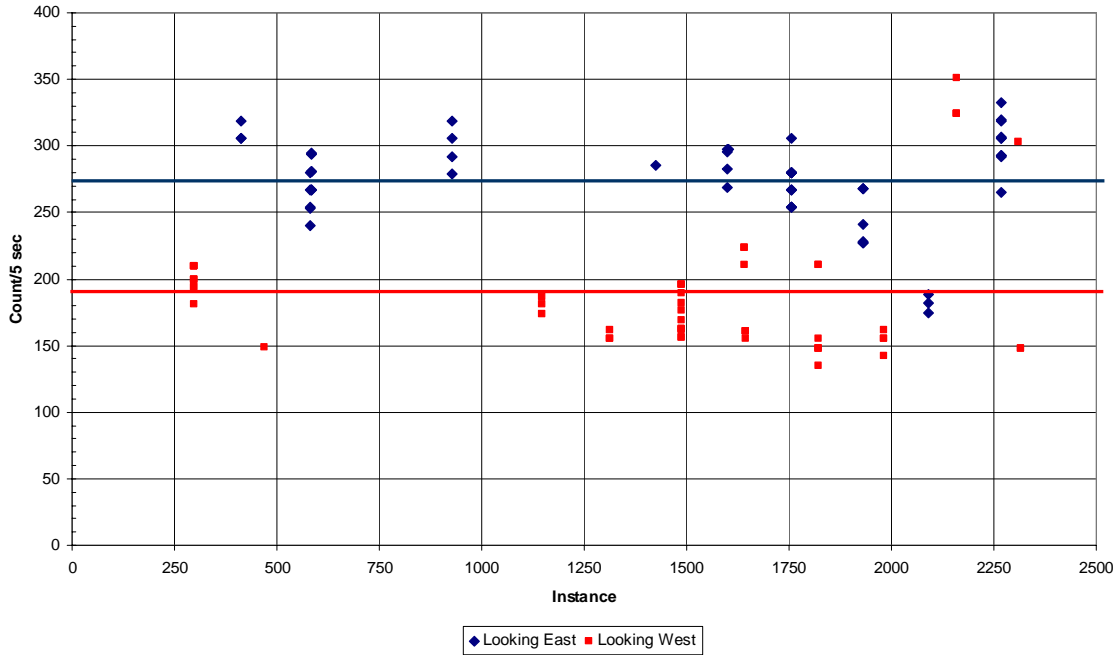
Figure C.1: Measured T6 values and date of measurement (1 Jan 00 = Day 1) for the geodetic bin at -30° Lat, 315° Long, 1000 km altitude showing average east-looking value (solid red line) and average west-looking value (solid blue line)

In either case, the resulting deviations between the data point and the measured average is the result of a random behavior within the proton fluxes themselves. Still, the random behaviors take the form of variations from some definite average value. This indicates that the correct statistical approach to use is to consider the east and west fluxes as individual Poisson distributions since the Poisson distribution "describes the results of experiments in which we count events that occur at random but at a definite average rate" [Taylor, 1997]. The combined average of east and west measurements is not a Poisson distribution, however, since the East-West Effect is not a random statistical process.

As an example, consider the data from the T6 channel of the -30Lat, -45° Long, 1000 km altitude bin. This data bin contained 122 lines of data, of which 11 were eliminated because they corresponded to dates when a solar proton event occurred. Of the surviving data, 55 entries

corresponded to measurements looking west while 56 entries corresponded to measurements looking east. Each entry lists the number of protons detected (or "counts") by CEASE during the preceding 5-second period.

For the given dataset, the sum of west-looking counts was 10475 particles and the sum of east-looking counts was 15368 particles. Dividing these numbers by the number of east and west instances yielded the following pre-error results.

$$j_e = \frac{10475}{55} = 190.5 \qquad\qquad\qquad\qquad \text{(C.1)}$$

$$j_w = \frac{15368}{56} = 274.4 \qquad\qquad\qquad\qquad \text{(C.2)}$$

Since the individual east and west fluxes can be described by a Poisson distribution, the error formula for a Poisson distribution should be applied to the measured counts. In this case, the appropriate error to use is simply the square root of the total east or west measured counts [Taylor, 1997], or $\sigma_e = \sqrt{\sum n_e}\big/ i_e$ and $\sigma_w = \sqrt{\sum n_w}\big/ i_w$, where σ_e and σ_w represent the errors of the eastward and westward average fluxes respectively, Σn_e and Σn_w represent the sum of all the east and west counts in the databin, and i_e and i_w represent the total number of measurements taken for both east and west cases. Applied to our example, this yielded the following:

$$\sigma_e = \frac{\sqrt{10475}}{55} = 1.861 \qquad\qquad\qquad\qquad \text{(C.3a)}$$

$$\sigma_w = \frac{\sqrt{15368}}{56} = 2.214 \qquad\qquad\qquad\qquad \text{(C.3b)}$$

$$j_e = 190.5 \pm 1.861 \qquad\qquad\qquad\qquad \text{(C.4a)}$$

$$j_w = 274.4 \pm 2.214 \qquad\qquad\qquad\qquad \text{(C.4b)}$$

Since the desired goal is the ratio j_e/j_w, it is necessary to combine σ_e and σ_w such that the ratio error σ_{ratio} can be determined. In this case, the appropriate technique to use is addition in quadrature. This is because both the east and west errors are being caused by random events independent of each other. Because of this, it is possible for the two errors to partially cancel each other out producing a closer outcome than either could have independently. The normal error propagation rule for quotients does not take this into account leading to the use of addition in quadrature.

In this case the appropriate equation for addition in quadrature is

$$\sigma_{ratio} = \frac{\sum n_e}{\sum n_w} \sqrt{\left(\frac{\sqrt{\sum n_e}}{\sum n_e}\right)^2 + \left(\frac{\sqrt{\sum n_w}}{\sum n_w}\right)^2} \tag{C.5}$$

which can be reduced to the following:

$$\sigma_{ratio} = \frac{\sum n_e}{\sum n_w} \sqrt{\frac{1}{\sum n_e} + \frac{1}{\sum n_w}} \tag{C.6}$$

Applying the numbers from our example to the equation results in a ratio error of

$$\sigma_{ratio} = \frac{10475}{15368} \sqrt{\frac{1}{10475} + \frac{1}{15368}} = .00864 \tag{C.7}$$

Combining this to the ratio of average j_e over average j_w produces a final result of

$$\frac{j_e}{j_w} = \frac{190.5}{274.4} \pm \sigma_{ratio} = 0.6940 \pm .00864 \, .$$

Bibliography

Armstrong, T.W., Colborn, B.L., and Watts, J.W. (1990), Characteristics of Trapped Proton Anisotropy at Space Station Freedom Altitudes, Report No. SAIC-90/1474, Science Applications International Corporation, Prospect, Tennessee

Badhwar, G.D., Kushin, V.V., Akatov, Yu A., and Myltseva, V.A. (1999), Effects of trapped proton flux anisotropy on does rates in low Earth orbit, *Radiation Measurements*, 30, 415-426

Badhwar, G.D., Atwell, W., Reitz, G., Beaujean, R., and Heinrich, W. (2002), Radiation measurements on the Mir Orbital Station, *Radiation Measurements*, 35, 393-422

Brautigam, D.H., Dichter, B.K., Ray, K. P., Turnbull, W.R., Madden, D., Ling, A., Holeman, E., Redus, R.H., and Woolf, S. (2001), Solar Cycle Variation of Outer Belt Electron Dose at Low-Earth Orbit, *IEEE Transactions on Nuclear Science*, 48, 2010-2015

Brautigam, D., Dichter, B., Woolf, S., Holeman, E., Ling, A., and Wrazen D. (2006), "Compact Environmental Anomaly Sensor (CEASE): Response Functions", technical report AFRL-VS-HA-TR-2006-1030, Air Force Research Lab, Hanscom AFB, MA

Cravens, T.E. (1997), *Physics of Solar System Plasmas,* pg. 7, Cambridge University Press, Cambridge, U.K.

Dachev, T., Atwell, W., Semones, E., Tomov, B., and Reddell, B. (2006), Observations of the SAA radiation distribution by Liulin-E094 instrument on ISS, *Advances in Space Research*, 37, 1672-1777

Daly, E.J., Lemaire, J., Heynderickx, D., and Rodgers, D.J. (1996), Problems with Models of the Radiation Belts, *IEEE Transactions on Nuclear Science*, 43, 403-415

Heckman H.,H. and Nakano, G.H. (1963), East-West Asymmetry in the Flux of Mirroring Geomagnetically Trapped Protons, *Journal of Geophysical Research*, 68, 2117-2120

Hedin, A.E. (1983), A Revised Thermospheric Model Based on Mass Spectrometer and Incoherent Scatter Data: MSIS-83, *Journal of Geophysical Review,* 88, pp 10170-10188

Hedin, A.E. (1987), MSIS-86 Thermospheric Model, *Journal of Geophysical Review,* 92, pp 4649-4662

Hedin, A.E. (1991), Extension of the MSIS Thermosphere Model into the Middle and Lower Atmosphere, *Journal of Geophysical Review,* 96, pp 1159-1172

Heirtzler, J.R. (2002), The Future of the South Atlantic Anomaly And Implications for Radiation Damage in Space, *Journal of Atmospheric and Solar-Terrestrial Physics, 64,* 1701-1708

Heirtzler, J.R. (1999), The geomagnetic field and radiation in near-earth orbits, technical report NASA/TM-1999-209481, Goddard Space Flight Center, Greenbelt, MD*, 64*

Heynderickx, D. (1995), Comparison between methods to compensate for the secular motion of the South Atlantic Anomaly, *Radiation Measurements*, 26,369-373

Konradi A., *et al.* (1994), Recent Space-Shuttle Observations of the South Atlantic Anomaly and the Radiation Belt Models, *Advances in Space Research*, 14, 915

Lenchek, A.M., and Singer, S.F. (1962), Effects to the Finite Gyroradii of Geomagnetically Tapped Protons, *Journal of Geophysical Research*, 67, 4073-4075

Redus, R.H., et al. (2004), "Small On-Board Environmental Diagnostic Sensors Package (SOBEDS)", technical report AFRL-VS-HA-TR-2004-1194, Air Force Research Lab, Hanscom AFB, MA

Rees, M.H. (1989), *Physics and chemistry of the upper atmosphere*, pp 25, 249, 253, Cambridge University Press, Cambridge, UK

Sakaguchi, T., Doke, T., Hayashi, T., Kikuchi, J., Hasebe, N., Kashiwagi, T., Takashima, T., Takahashi, K., Nakano, T., Nagaoka, S., Takahashi, S., Yamanaka, H., Yamaguchi, K., and Badhwar, G.D. (1997), Radiation dosimetry measurements with real time radiation monitoring devices (RRMD)-II in space shuttle STS-79, *Japanese Journal of Applied Physics, Part I: Regular Papers & Short Notes & Review Papers*, 36, 7453-7459

Schunck, R., and Nagy, A. (1999), *Ionospheres - Physics, Plasma Physics, and Chemistry,* pp. 67, 82-83, Cambridge University Press, Cambridge, UK

Sturrock, P. (1994), *Plasma Physics*, pp 40, Cambridge University Press, Cambridge, UK

Taylor, J.R. (1997), *Introduction to Error Analysis*, pp 49-53, 60-61, 245-252, University Science Books, Sausalito, CA

Walt, M. (1994), *Introduction to geomagnetically trapped radiation*, pg 61, Cambridge University Press, Cambridge, N.Y.

Vita

Captain Shaun M. Easley graduated from Suncoast Community High School in Riviera Beach, FL in the top 10 of the school's rigorous Math, Science & Engineering (MSE) magnet program in June of 1998. His outstanding achievement in high school earned him a four-year AFROTC scholarship that he used to attend Embry-Riddle Aeronautical University in Daytona Beach, FL. In April of 2002, he graduated with a Bachelor of Science degree in Engineering Physics and was promptly commissioned as a second lieutenant through the AFROTC Detachment 157 at Embry-Riddle.

His first assignment was to the Space Vehicles directorate of the Air Force Research Lab (AFRL/VS) at Kirtland AFB, NM. While there, he was given the opportunity to be part of a unique organization known as Space CHOP, whose purpose is to find vulnerabilities to U.S. space assets from rogue nation and/or terrorist organizations. Halfway through his assignment at Kirtland, he was selected as the Deputy Program Manager for a $120M+ research & development satellite being stood up by AFRL/VS. In September 2005 he entered the Graduate School of Engineering and Management, Air Force Institute of Technology to attain a Master's degree in Applied Physics. Upon graduation, he will be assigned to the Air Force Technical Applications Center at Patrick AFB, FL.

REPORT DOCUMENTATION PAGE

1. REPORT DATE *(DD-MM-YYYY)* 01-09-2007	2. REPORT TYPE Master's Thesis	3. DATES COVERED *(From – To)* Jun 2006 – Mar 2007

4. TITLE AND SUBTITLE	5a. CONTRACT NUMBER
Anisotropy in the South Atlantic Anomaly	5b. GRANT NUMBER
	5c. PROGRAM ELEMENT NUMBER

6. AUTHOR(S)	5d. PROJECT NUMBER
Easley, Shaun M.., Captain, USAF	5e. TASK NUMBER
	5f. WORK UNIT NUMBER

7. PERFORMING ORGANIZATION NAMES(S) AND ADDRESS(S) Air Force Institute of Technology Graduate School of Engineering and Management (AFIT/EN) 2950 Hobson Way WPAFB OH 45433-7765	8. PERFORMING ORGANIZATION REPORT NUMBER AFIT/GAP/ENP/07-02

9. SPONSORING/MONITORING AGENCY NAME(S) AND ADDRESS(ES) AFRL/VSBX Attn: Dr. Greg Ginet 29 Randolph Rd. Hanscom AFB, MA 01731 DSN: 478-3974	10. SPONSOR/MONITOR'S ACRONYM(S)
	11. SPONSOR/MONITOR'S REPORT NUMBER(S)

12. DISTRIBUTION/AVAILABILITY STATEMENT
      APPROVED FOR PUBLIC RELEASE; DISTRIBUTION UNLIMITED.

13. SUPPLEMENTARY NOTES

14. ABSTRACT
        From June 2000 through July 2006, the TSX-5 satellite measured proton fluxes in the Earth's magnetosphere using its CEASE instrument. A review of the satellite data by scientists at AFRL/VSBX revealed an unanticipated, recurring bi-modal structure in histograms of the proton counts. This research identified the bi-modal behavior as anisotropic in nature, and the result of two separate processes. At low altitudes the anisotropy was well described by the classic "East-West Effect." Comparisons of the satellite data to simple analytical models are presented. At high altitudes, the anisotropy was the result of the detector measuring protons at different pitch angles when looking east vs. west. The sampled pitch angles were also found to be function of location, leading to a latitudinal variation to this anisotropy. Finally, we also examined a series of unusually high readings that affected some of the statistics in this study. These anomalous counts were found to have a possible solar cycle dependence leading to questions about the suitability of the current time-independent scheme used to sort the satellite's data set. Other possible explanations for the anomalous counts are also presented.

15. SUBJECT TERMS
   Space Weather, South Atlantic Anomaly, East-West Effect, Anisotropy, Pitch Angle Distribution,
   Tri-Service eXperiment-5 (TSX-5), Compact Environmental Anomaly SEnsor (CEASE),
   IGRF, MSIS

16. SECURITY CLASSIFICATION OF:			17. LIMITATION OF ABSTRACT	18. NUMBER OF PAGES	19a. NAME OF RESPONSIBLE PERSON Christopher G. Smithtro, Maj., USAF (ENP)
REPORT U	ABSTRACT U	c. THIS PAGE U	UU	98	19b. TELEPHONE NUMBER *(Include area code)* (937) 255-3636, ext 4505; e-mail: Christopher.Smithtro@afit.edu